remote sensing

MDPI

Article

An Autoregressive Steady-State Compensation Method for Cross-Correlation Interference Suppression in GPS-Based Passive Radar

Fan Xu [1], Chenghao Jiang [2,*], Shiyang Tang [1], Feng Luo [1,2], Linrang Zhang [1], Xianxian Luo [2] and Zixuan He [1]

[1] National Laboratory of Radar Signal Processing, Xidian University, Xi'an 710071, China; fanxu_xd@stu.xidian.edu.cn (F.X.); sytang@xidian.edu.cn (S.T.); luofeng@xidian.edu.cn (F.L.); lrzhang@xidian.edu.cn (L.Z.); 21021110329@stu.xidian.edu.cn (Z.H.)
[2] Hangzhou Institute of Technology, Xidian University, Hangzhou 311231, China; luoxianxian@xidian.edu.cn
* Correspondence: jiangchenghao@xidian.edu.cn

Highlights

What are the main findings?

- By introducing an autoregressive backward-extrapolation strategy to compensate convergence-stage frequency estimation errors, the proposed autoregressive steady-state compensation (ARSSC) method achieves up to 7.4 dB interference suppression ratio (ISR) improvement over conventional reconstruction approaches in simulation, and an ablation study confirms a 14.5 dB advantage over polynomial extrapolation.
- Real-data experiments under different field scenarios yield a 6.3 dB ISR improvement over traditional reconstruction, and the airport aircraft case raises the detection probability from 17.6% to over 99% at $P_{fa} = 10^{-4}$.

What are the implications of the main findings?

- Since mainlobe interference from multiple Global Navigation Satellite System (GNSS) satellites is prevalent and unavoidable in passive bistatic radar (PBR) for aerial target detection, the ARSSC framework addresses a fundamental performance bottleneck, substantially expanding the feasible surveillance coverage of GNSS-based PBR systems.
- The data-driven autoregressive (AR) compensation strategy requires no prior knowledge of noise statistics, offering a lightweight and generalizable solution for frequency estimation error correction in GNSS-based passive radar signal reconstruction.

Abstract

GPS-based passive bistatic radar (PBR) benefits from global satellite coverage for target surveillance. However, multiple GPS satellites within the PBR mainlobe generate cross-correlation interference (CCI) that severely masks target echoes, reducing the detection probability to zero across significant portions of the surveillance area. Existing reconstruction-based suppression methods rely on iterative frequency estimation, which introduces substantial errors during the convergence stage of the tracking loop, leading to degraded interference suppression performance. This paper proposes an autoregressive steady-state compensation (ARSSC) method to address this limitation. First, a precise carrier frequency estimation model is established to accelerate convergence and improve tracking accuracy. Second, the frequency estimation outputs are partitioned into convergence and steady-state stages, and a p-th order autoregressive (AR) model is fitted to the steady-state estimates. A compensation function is then derived from the AR model to

Check for updates

Academic Editors: Gino Dardanelli and Chen Wang

Received: 10 April 2026
Revised: 21 May 2026
Accepted: 22 May 2026
Published: 27 May 2026

Copyright: © 2026 by the authors. Licensee MDPI, Basel, Switzerland. This article is an open access article distributed under the terms and conditions of the Creative Commons Attribution (CC BY) license.

correct the frequency errors in the convergence stage. Finally, the compensated reconstructed CCI signals are used to construct an interference subspace, and a projection-based algorithm suppresses the CCI from the surveillance signal. Simulation results demonstrate that the proposed ARSSC method achieves a maximum interference suppression improvement of 7.4 dB compared to conventional reconstruction approaches. Real-data experiments conducted under different field scenarios further validate the method, yielding a 6.3 dB interference suppression ratio (ISR) improvement over traditional reconstruction techniques in both tested cases.

Keywords: cross-correlation interference suppression; passive bistatic radar; GPS; autoregressive model; frequency estimation; mainlobe interference

1. Introduction

Passive bistatic radar (PBR) systems utilize non-cooperative illumination as the radar transmitter and operate in a silent receiving mode. Without a high-power transmitter or heavy power supply, PBR is considered one of the most covert and maneuverable radar systems. With the rapid increase in satellite numbers, the research focus of PBR has shifted from ground-based to space-based illuminators. In particular, Global Positioning System (GPS)-based passive bistatic radar (GPBR) has received considerable attention for its extensive illumination coverage [1] and simultaneous irradiation from multiple satellites, which enhances its advantages in aerial and open-sea surveillance [2,3]. These characteristics position GPBR as a promising passive remote sensing modality for air traffic monitoring, border surveillance, and wide-area observation without dedicated transmission infrastructure, complementing concurrent advances in active radar systems and radar-communication networks [4,5].

A primary characteristic of GPBR is the extremely low power density of satellite signals at ground level. To overcome this inherently low signal power, long coherent integration is generally required to achieve an adequate signal-to-noise ratio for target detection. Such extended observation windows, however, introduce non-negligible range walk and Doppler migration, for which various compensation techniques have been developed [6–9]. Precise models have also been established to address the phase mismatch effect in moving target detection [10,11]. Multi-source fusion techniques have also been proposed to further increase target signal power [12]. However, the multi-satellite feature also introduces direct-path interference (DPI) and deliberate directional interference. The DPI can be mitigated through sidelobe cancellation (SLC) and sidelobe blanking (SLB) [13–15], while blind source separation-based approaches such as independent component analysis (ICA) [16–23] have been proposed for the latter. Yet, all the aforementioned studies focus on sidelobe or directional interference, leaving another critical interference mechanism largely unexamined: the cross-correlation interference generated by simultaneously receiving multiple satellite signals within the surveillance antenna mainlobe.

This interference, termed cross-correlation interference (CCI), has received comparatively little attention despite its severe impact on air target detection. As shown in Figure 1, signals from all satellites within the mainlobe are amplified by the antenna and subsequently generate CCI; these satellites are referred to as interference satellites. The CCI masks the target with a significantly higher power level and is further amplified by both the receiving antenna and the coherent integration process. Unlike conventional interference, CCI occupies broad swaths of the range-Doppler plane, ultimately reducing the detection probability to zero. As analyzed in Section 2, the received signal-to-interference ratio

(SIR) can drop below −47 dB under typical satellite geometries, rendering over 20% of the surveillance area undetectable.

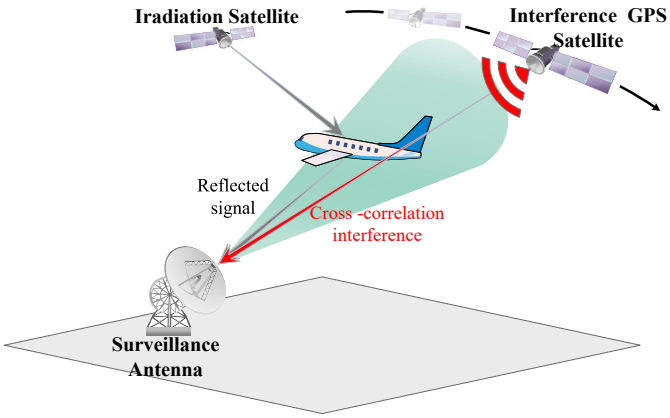


Figure 1. Configuration of GPS-based PBR.

To address mainlobe CCI in aircraft detection, one approach relies on blind source separation. The equivariant adaptive separation via independence (EASI) algorithm [24] models the received signal as a linear combination of CCIs and target signals, recovering original signals via expectation–maximization for mixing matrix estimation. However, EASI suffers from ordering and amplitude uncertainty [25], and its performance degrades significantly when the signal-to-noise ratio (SNR) falls below 10 dB [26]—a common condition for GPS signals at ground level. Another category of existing methods employs prior structural knowledge for signal reconstruction. Schmidt et al. [27] demonstrated the feasibility of exploiting GPS signal structure for interference cancellation on a real-time software-defined radio receiver. Building upon this concept, Zheng et al. [28] utilized the software radio platform (SRP) to achieve coherent reconstruction of interference waveforms and cancellation via orthogonal projection [29]. Zhang et al. [30] proposed a joint low-rank and sparse recovery method, but it requires multi-channel spatial diversity unavailable in single-channel PBR.

However, reconstruction-based methods share a critical limitation: the phase-locking loop (PLL) requires a convergence period during which the frequency estimates contain significant errors, yet existing SRP-based approaches directly use these raw estimates without any compensation. As demonstrated in [31], the coherent observation time for an aircraft at 10 km range is less than 0.64 s, while the convergence stage wastes a substantial portion of this valuable time, severely degrading the suppression performance (see Section 2.3). Compensating these errors is itself non-trivial, because the tracking-loop output superimposes the true satellite Doppler trajectory—a smooth polynomial due to orbital mechanics [32]—with colored noise introduced by the loop filter dynamics. Polynomial fitting captures only the deterministic component and ignores the temporal correlation of the tracking noise, leading to divergent backward extrapolation (see Section 4.1). Kalman filtering could in principle model both components, but requires explicit specification of the process and measurement noise covariances, which vary with the interference-to-noise ratio (INR) and satellite geometry and are difficult to calibrate in practice. These limitations motivate the use of autoregressive (AR) modeling, which is purely data-driven: it captures the frequency trend via ordinary least squares [33], without prior knowledge of noise statistics, making it well suited for multi-satellite CCI suppression.

In this paper, to address the performance limitation caused by frequency estimation errors in CCI suppression, an autoregressive steady-state compensation (ARSSC) method is proposed. The main contributions of this work are summarized as follows:

1. A precise carrier frequency estimation model is established that accelerates the convergence of the tracking loop and provides high-accuracy steady-state estimates as the data foundation for subsequent AR modeling.
2. An ARSSC-based compensation method is proposed, which partitions the frequency estimation outputs into convergence and steady-state stages, fits the steady-state estimates with a p-th order AR model, and derives a backward-extrapolation compensation function to correct the frequency errors during the convergence stage.
3. A subspace projection-based suppression algorithm is developed that utilizes the compensated reconstructed CCI signals to construct an interference subspace, enabling effective CCI cancellation from the surveillance signal.

The effectiveness of the proposed method is validated through both simulations and real-data experiments at Xi'an Xianyang International Airport, with detailed results presented in Section 4.

The rest of this paper is organized as follows. Section 2 establishes a geometric modeling framework for passive radar systems under multiple CCI conditions. Based on this model, the impact of interference on radar detection, as well as the degradation of interference suppression performance caused by estimation errors, is analyzed. Next, an estimation-and-suppression method with the ARSSC compensation algorithm is proposed in Section 3. Section 4 presents numerical results from computer simulations and real-data experiments. Section 5 discusses the robustness of the proposed method to receiver platform motion and maneuvering targets. Finally, conclusions are drawn in Section 6.

2. Signal Model and Analysis

In this section, the received signal model with multiple CCI is established, followed by analysis of interference impact from the signal reception to detection stages. To further identify the factors contributing to the performance degradation of conventional methods, the effects of frequency errors, amplitude errors, and phase errors on the results are analyzed.

2.1. Signal Model

Figure 2 shows the GPBR system in a local (O-XYZ) reference frame centered at the receiver R_x. Let $T_{x,0}$ denote the radar transmitter and $T_{x,k}$ $(k = 1, \ldots, K)$ the remaining GPS satellites within the surveillance beam. The position and velocity vectors of the k-th satellite, the target, and the receiver are denoted as $(T_{x,k}, v_k)$, (T_A, v_A), and (R_x, v_R), respectively.

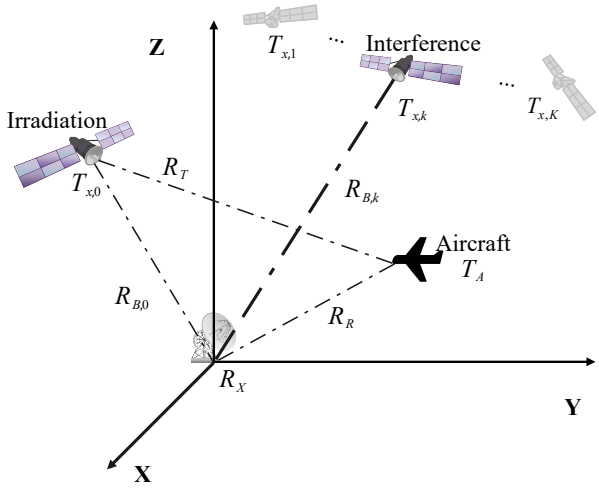


Figure 2. GPS-based PBR system geometry.

The signal transmitted by the k-th satellite is

$$s_k(t) = C_k(t)D_k(t)\exp(j2\pi f_c t) \tag{1}$$

where C_k is the pseudorandom and periodic ranging code of the k-th satellite, $D_k(t)$ is the navigation message, and f_c is the carrier frequency of the transmitted signal. Throughout this work, the GPS L1 Coarse/Acquisition (C/A) signal is considered, with $f_c = 1575.42$ MHz, consistent with the experimental setup described in Section 4.4.

Due to the relative motion between the satellite and receiver, Doppler shift $f_{d,k}$ is introduced in the directly received GPS signal. Accordingly, after down-conversion, the baseband direct GPS signal can be expressed as

$$s_{d,k}(t) = A_k(t)C_k(t-\tau_k)D_k(t-\tau_k)\exp(j2\pi f_{d,k}t) \tag{2}$$

where A_k $(k = 1, 2, \ldots, K)$ is the complex amplitude that encapsulates the range attenuation and the carrier-dependent propagation phase $\exp(-j2\pi f_c\tau_k)$, and τ_k is the signal delay from the k-th satellite to the receiver.

The bistatic range $R_{\text{tar}}(t)$, given by the range difference between 0-th satellite, target and receiver is written as

$$R_{\text{tar}}(t) = R_R(t) + R_T(t) - R_{B,0}(t) \tag{3}$$

where $R_R(t) = |T_A - R_x|$ is the line-of-sight range between the target and the receiver, $R_T(t) = |T_{x,0} - T_A|$ is the distance between the illuminator with the 0-th satellite and the target, and $R_{B,0}(t) = |T_{x,0} - R_x|$ refers to the baseline between the transmitter and the receiver. Hence, the baseband target signal is

$$\begin{aligned} s_{\text{tar}}(t) = {} & A_{\text{tar}}C_0(t-\tau_{\text{tar}})D_0(t-\tau_{\text{tar}}) \\ & \times \exp\{j2\pi[f_{d,0}t - (f_{d,0}+f_c)\tau_{\text{tar}}]\} \end{aligned} \tag{4}$$

where A_{tar} is the complex amplitude, and $\tau_{\text{tar}} = [R_T(t) + R_R(t)]/c$ is the bistatic time delay. Therefore, the expression of the remaining signal received by the surveillance channel is

$$r_{surv}(t) = s_{\text{tar}}(t) + \sum_{k=1}^{K} s_{d,k}(t) \tag{5}$$

The direct signal from the 0-th satellite, mitigated via SLC/SLB [13–15], is excluded from (5) and serves as the reference signal r_{ref}.

Then pulse compression is realized through delay-Doppler cross correlation function of the ranging code between reference signal and reflected target signal. T_0 is set as the global observation time, the pulse compression can be obtained by

$$R_p(t) = \int_{-\infty}^{+\infty} r_{surv}(\tau)r_{ref}^*(t-\tau)d\tau \tag{6}$$

Substituting (4), (5) and $r_{ref} = s_{d,0}$ into (6), the cross correlation is rewritten as

$$\begin{aligned} R_p(t) = {} & \alpha_{\text{tar}}\Lambda[t-\tau_{\text{tar},0}] \times \exp[-j2\pi f_c\tau_{\text{tar},0}] \\ & + \sum_{k=1}^{K} \beta_k\Theta_k[t-\tau_{k,0}] \times \exp[-j2\pi f_{d,k}\tau_{k,0}] \end{aligned} \tag{7}$$

where α_{tar} and β_k are the composite correlation amplitudes of the target and the k-th interference signal, respectively, $\Lambda(\cdot)$ is the auto-correlation function between the reference

and reflected signal, $\Theta_k(\cdot)$ is the cross-correlation function between the reference and interference signal, $\tau_{\text{tar},0} = \tau_{\text{tar}} - \tau_0$ and $\tau_{k,0} = \tau_k - \tau_0$ are the differential delays of the target signal and CCI signal with respect to the reference, respectively.

2.2. Interference Impact Analysis

To visualize the formation process of the results discussed, Figure 3 illustrates the block diagram of interference signal reception in a passive radar system. After pulse compression, the amplitude of the reflected target signal is significantly weaker than that of the noise-like CCI. Consequently, the CCI severely degrades the equivalent output SNR and detection probability compared to other interference types. As this interference originates from the cross-correlation between the jamming signal and the reference signal, it is hence termed cross-correlation interference.

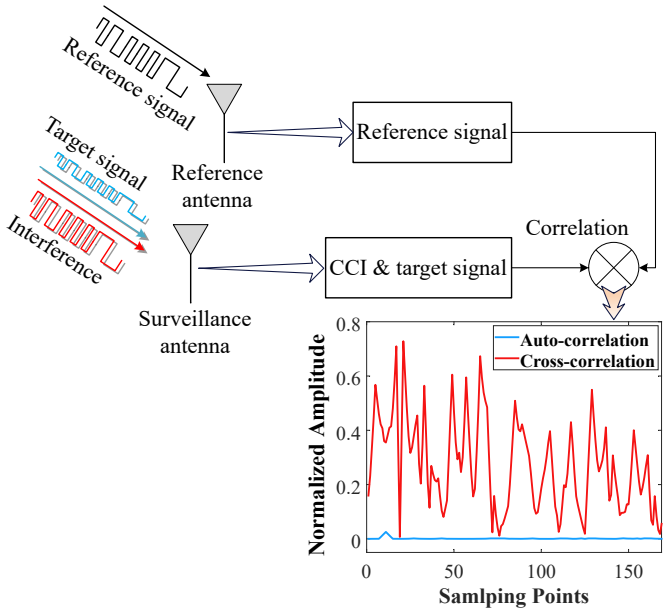


Figure 3. Cross-correlation effect of target echo in signal processing.

To evaluate the received CCI strength, a simulation analyzes the SIR as the surveillance antenna direction varies from horizontal to vertical, with an aircraft at 1 km range. According to the free-space path loss model, the interference power from the k-th satellite is

$$P_{i,k} = \text{EIRP} \times \frac{A_r G_k}{4\pi R_{i,k}^2} \tag{8}$$

where the effective isotropic radiated power (EIRP) is 26.6 dBW for GPS satellites, A_r and G_k are the effective aperture area and receive antenna gain, and $R_{i,k}$ is the satellite-to-receiver range. It should be noted that the free-space path loss model is used here as a first-order approximation for quantifying the CCI impact. Real-world propagation effects, including atmospheric attenuation, ionospheric delay, and ground-reflected multipath, may introduce deviations in the received amplitude, phase, and delay. The real-data experiments in Section 4.4 inherently include these propagation effects and are therefore used to further validate the practical effectiveness of the proposed suppression method. The target signal power is

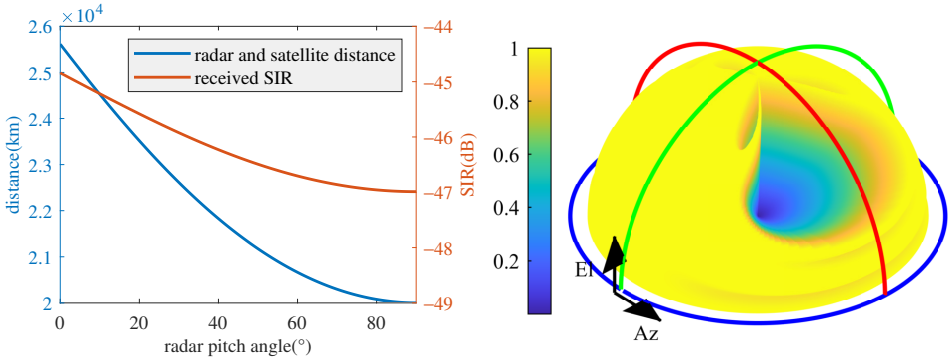
$$P_r = \text{EIRP} \times \frac{A_r G_r \sigma}{(4\pi)^2 R_T^2 R_R^2} \tag{9}$$

where σ is the bistatic radar cross section (RCS). As illustrated in Figure 4a, the SIR drops to -47 dB at high elevation angles. Since auto-correlation peaks are 21 dB above cross-

correlation peaks under equal input power [34], the target echo is significantly weaker than CCI after correlation processing. The equivalent output SNR_0 determines the detection probability P_D:

$$\begin{cases} P_D \approx 0.5 \times \mathrm{erfc}\left(\sqrt{-\ln P_{fa}} - \sqrt{\mathrm{SNR}_0 + 0.5}\right) \\ \mathrm{erfc}(z) = 1 - \frac{2}{\sqrt{\pi}} \int_0^z e^{-v^2} dv \end{cases} \tag{10}$$

where P_{fa} is the radar false alarm rate. To illustrate the severity of CCI, a representative scenario is considered: a surveillance antenna with a half-power beamwidth of 28° and a single CCI source located at 45° azimuth and 45° elevation. Under this configuration, Figure 4b shows that the detection probability falls to zero over a wide angular range, rendering 20.12% of the evaluated angular surveillance area undetectable. This percentage depends on the specific antenna pattern and CCI geometry; the analysis here serves to quantify the scale of the problem under a typical GPBR configuration.



(**a**) (**b**)

Figure 4. CCI impact on detection performance. (**a**) Distance and SIR versus pitch angle. (**b**) Target detection probability with azimuth and elevation in CCI scenario.

To identify the input INR boundary below which the CCI ceases to impact target detection, the following analysis is conducted. For the typical detection case (EIRP = 26.6 dBW, $G_r \approx +16$ dBi), with coherent integration time $T_{\mathrm{coh}} = 0.25$ s, a GPS C/A cross-correlation isolation of ≈21 dB between distinct PRNs, and the traditional SRP-based reconstruction saturating at an ISR of ≈13 dB, the residual CCI in the target's range-Doppler (RD) cell satisfies

$$\mathrm{INR}_{\mathrm{RD,residual}} = \mathrm{INR}_{\mathrm{in}} + 10\log_{10}(B\,T_{\mathrm{coh}}) - 21 - 13. \tag{11}$$

Setting $\mathrm{INR}_{\mathrm{RD,residual}} \leq 0$ in (11) (residual buried in the noise floor, no measurable change in P_D through Equation (10)) yields the critical input boundary $\mathrm{INR}_{\mathrm{in,crit}} \approx -20$ dB: below this level the CCI is operationally inactive and active suppression is unnecessary. The GPS link budget normally yields an input $\mathrm{INR}_{\mathrm{in}} \approx 0$ dB; although this value fluctuates with the receive-antenna gain, pattern nulls, and atmospheric attenuation, in most operational scenarios the resulting INR remains well above the −20 dB boundary and the CCI cannot be ignored.

2.3. Limitations of Conventional Reconstruction Methods

Conventional SRP-based reconstruction techniques have shown some effectiveness in suppressing strong GPS signals [28,30], but the accuracy of the reconstructed signal parameters critically determines suppression performance. To analyze the influencing factors, controlled simulations are conducted with noise-free GPS interference signals. The ISR is evaluated by adjusting parameter offsets, as plotted in Figure 5. A frequency offset of just 2 Hz causes the ISR to drop drastically to 41 dB, highlighting the extreme sensitivity to frequency estimation errors.

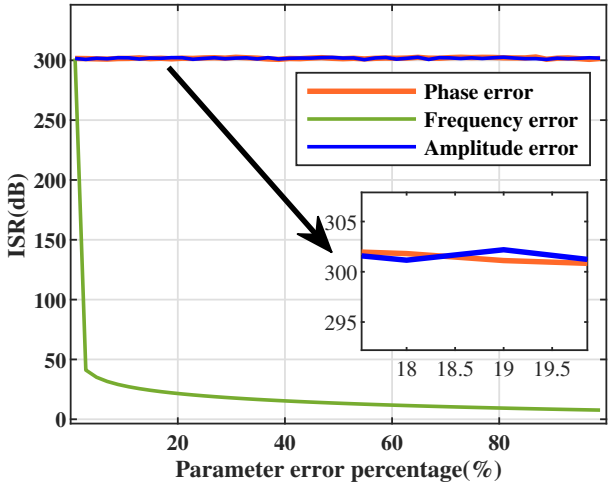


Figure 5. ISR versus parameter error.

The results from 1000 Monte Carlo experiments shown in Figure 6 highlight the frequency estimation process and its impact on ISR during the estimation period. The entire estimation period can be divided into two stages based on the frequency estimation errors. The initial stage is characterized by a high error rate, which occurs during the convergence period of the tracking loop. This phase lasts for approximately 50 ms. After that, the tracking loop stabilizes, and the error reduces significantly, leading to more accurate frequency estimation. The significant errors in the initial stage lead to a deterioration of the suppression effect throughout the entire stage, and the ISR decreases substantially from its ideal value of 23.83 dB (corresponding to no frequency error) to 15.37 dB, resulting in a reduction of 8.46 dB.

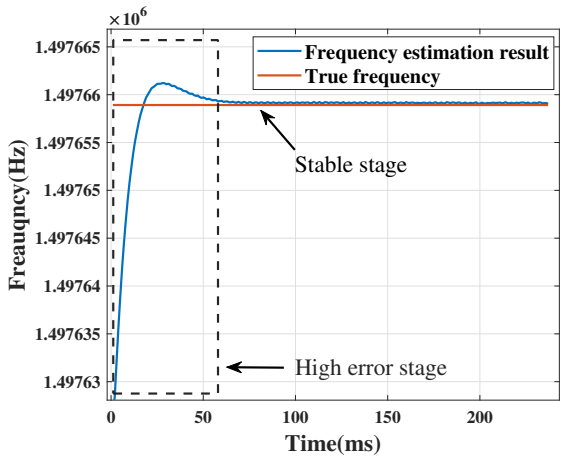


Figure 6. SRP output frequency estimate at INR = 20 dB. Based on the frequency estimation result shown in the blue line, ISR decreases from 23.83 dB to 15.37 dB.

This analysis confirms that frequency estimation errors during convergence are the dominant factor degrading ISR, and their compensation is the key to performance improvement.

3. Approach

To effectively improve the CCI suppression performance, an interference suppression approach is proposed in this section, which is mainly divided into two steps. The first step is CCI signal reconstruction. Subsequently, to compensate for the frequency estimation error, an ARSSC-based suppression method is proposed, which identifies the steady-state frequency and utilizes the AR fitting model to correct the frequency during the convergence stage.

3.1. Iterative Interference Reconstruction

As modeled in (5), both the quantity and source of received CCI signals are unknown. Hence, initial value analysis is first performed to provide initial parameters for subsequent processing and estimate the number of CCI sources.

The surveillance signal in (5) is sampled with a sampling frequency f_s and cross-correlated with 32 local ranging codes. For notational brevity, the Doppler frequency $f_{d,k}$ is hereafter denoted as f_k. The discrete interference signal from the k-th satellite is denoted as

$$\begin{aligned} y_k(n) &= C_k(n-\tau_k)D_k(n-\tau_k) \\ &\quad \times \exp(j2\pi f_k(n-\tau_k)+\varphi_k) \end{aligned} \tag{12}$$

where y_k is the CCI signal collected and sampled of duration T_0 at the surveillance channel, with the amplitude normalized to 1. After cyclic cross-correlation with the u-th $(1 \le u \le 32)$ local reference signal h_u^l of frequency f_l, the correlation results can be expressed as

$$R_k^u(l) = \frac{1}{N}\sum_{n=1}^{N} y_k(n)h_u^l(n)\exp(-j2\pi f_l n) \tag{13}$$

where N is the number of sampling points. Since neither the pseudo-random noise (PRN) code identity, the Doppler frequency, nor the code phase of the interference signals is known a priori, the initial parameter estimation requires a joint search across all three dimensions: the code delay $n_{\tau,k}$ (via the correlation lag), the Doppler frequency $f_{l_0,k}$ (via the frequency bins f_l), and the satellite/PRN index, which is determined by scanning the 32 local ranging codes and is denoted by k after detection. A correlation peak at the position $(n_{\tau,k}, f_{l_0,k}, k)$ indicates the presence of an interference signal. Therefore, the initial phase $\varphi_{k,0}$ and frequency $f_{k,0}$ for the subsequent precise parameter estimation can be calculated as

$$\begin{cases} \varphi_{k,0} = \dfrac{2\pi f_{l_0,k} n_{\tau,k}}{f_s} \\ f_{k,0} = f_{l_0,k} \end{cases} \tag{14}$$

Once the identification of the interference satellite is determined, the ranging code of the k-th satellite can be obtained, which provides envelope data C_k for subsequent precise parameter estimation.

The estimation of envelope and carrier is the key of interference reconstruction. Due to the continuous motion of satellites and atmospheric disturbances, the phase and frequency of interference signals remain in a constant state of change. As a result, an iterative interference parameter estimation method is employed to adjust the estimation results continuously, enabling dynamic tracking of interference parameters. The received CCI signals in (5) are segmented into N_t equivalent pulses with a repetition interval T_c equal to the ranging code period. Let $L_c = T_c f_s$ denote the number of samples per pulse. The segmented signals are multiplied with orthogonal local carrier signals to obtain In-Phase (I) and Quadrature (Q) branch outputs $r_{I,m}^k$ and $r_{Q,m}^k$, where $\Delta\varphi_{k,m}$ is the phase difference between the input and local carrier of the m-th pulse. After removing the double-frequency components via low-pass filtering, the carrier phase difference can be estimated as

$$\Delta\hat{\varphi}_{k,m} = \arctan\left(\frac{r_{Q,m}^k}{r_{I,m}^k}\right) \tag{15}$$

Although the navigation data cause a phase flip in CCI signals, the effect of this inversion is eliminated after (15). Consequently, the $(m+1)$-th local carrier phase can be obtained through the following iterative calculation

$$\varphi_{k,m+1} = \varphi_{k,m} - \Delta\hat{\varphi}_{k,m} \tag{16}$$

The dynamic carrier phase estimation method above allows for continuous estimation of the carrier phase of the CCI signals, and the carrier frequency estimation difference is

$$\begin{aligned}\Delta\hat{f}_k(m) = \Delta\hat{f}_k(m-1) \\ + \frac{32\zeta^2 B_L}{4\zeta^2+1} \times \frac{\hat{\varphi}_{k,m} - \hat{\varphi}_{k,m-1}}{\pi} + \kappa\frac{256 B_L \zeta^2}{(4\zeta^2+1)^2}\hat{\varphi}_{k,m}\end{aligned} \tag{17}$$

where $\Delta\hat{f}_k(m)$ is the frequency difference estimate between the true frequency and the local frequency based on the phase estimation result in (16), ζ is the loop damping ratio, B_L is the noise bandwidth of the loop filter, κ is the frequency-aided gain coefficient, and T_c is the time width of the C/A code. After that, the local frequency can be rewritten as

$$\hat{f}_k(m+1) = f_{k,0} + \Delta\hat{f}_k(m) \tag{18}$$

where $f_{k,0}$ is the initial frequency estimation result from (14).

For envelope tracking, a standard early-minus-late code discriminator is employed. The in-phase/quadrature (I/Q) branch signals are correlated with early (C_E), prompt (C_P), and late (C_L) code replicas, and the normalized discriminator output is

$$G_{k,m} = \frac{(I_{E,m}^2 + Q_{E,m}^2) - (I_{L,m}^2 + Q_{L,m}^2)}{(I_{E,m}^2 + Q_{E,m}^2) + (I_{L,m}^2 + Q_{L,m}^2)} \tag{19}$$

where $G_{k,m}$ represents the code phase error of the m-th pulse. The envelope phase is then updated iteratively as $\hat{\vartheta}_{k,m} = \hat{\vartheta}_{k,m-1} + G_{k,m}$.

Consequently, the interference signal can be reconstructed as

$$\hat{y}_k(n,m) = C_k(n+\hat{\vartheta}_{k,m})\, D_k(n+\hat{\vartheta}_{k,m}) \times \exp\left(j2\pi\hat{f}_k(m)n + \hat{\varphi}_{k,m}\right) \tag{20}$$

As shown in Algorithm 1, utilizing the initial parameters, dynamic estimation and further reconstruction can be implemented through N_t iterations.

Algorithm 1 Iterative Interference Reconstruction

Require: Surveillance signal r_{surv}, 32 local CA codes C_u $(u = 1, \ldots, 32)$
Ensure: Reconstructed interference signals $\hat{y}_k$ $(k = 1, \ldots, K)$
Cross-correlate r_{surv} with 32 local codes at different frequency bins f_l
Identify K interference satellites from correlation peaks at positions $(n_{\tau,k}, f_{l_0,k}, k)$
Obtain initial parameters: $\varphi_{k,0}$, $f_{k,0}$ from (14)
for $k = 1$ to K **do**
  Obtain ranging code C_k for the k-th satellite
  for $m = 0$ to N_t **do**
    Compute I/Q branches $r_{I,m}^k$, $r_{Q,m}^k$ using local carrier at $f_{k,m}$
    Low-pass filter to remove high-frequency components
    Estimate phase difference: $\Delta\hat{\varphi}_{k,m} = \arctan(r_{Q,m}^k / r_{I,m}^k)$
    Update carrier phase: $\varphi_{k,m+1} = \varphi_{k,m} - \Delta\hat{\varphi}_{k,m}$
    Update carrier frequency: $\hat{f}_k(m+1) = f_{k,0} + \Delta\hat{f}_k(m)$ via (17)
    Estimate envelope phase: $\hat{\vartheta}_{k,m} = \hat{\vartheta}_{k,m-1} + G_{k,m}$
    Reconstruct: $\hat{y}_k(n,m) = C_k(n+\hat{\vartheta}_{k,m})\, D_k(n+\hat{\vartheta}_{k,m}) \exp(j2\pi\hat{f}_k(m)n + \hat{\varphi}_{k,m})$
  end for
end for
return $\hat{y}_k$ $(k = 1, \ldots, K)$

3.2. ARSSC-Based Compensation and Suppression

After CCI reconstruction, the frequency discrepancy in (17) can be utilized to qualitatively characterize the estimation error of the derived frequency. To facilitate the determination of stable state boundaries, a moving average filter is used to remove the high-frequency jitter components of $\Delta\hat{f}_k$.

$$g(m) = \frac{1}{2w+1} \sum_{i=m-w}^{m+w} |\Delta\hat{f}_k(i)| \tag{21}$$

where $g(m)$ is the filtered estimation frequency discrepancy and $2w+1$ is the window length of the filter. The boundary of the steady state m_0 can be expressed as

$$\begin{cases} \min m_0 \\ \text{s.t. } g(m) \le \eta_f, \quad \forall\, m \ge m_0 \end{cases} \tag{22}$$

where η_f is the judgment threshold for steady state. The selection of η_f involves a trade-off between model fidelity and sample utilization; a detailed sensitivity analysis in Section 4.3.1 demonstrates that the method maintains robust performance over a broad range of $\eta_f \in [0.018, 0.024]$.

Once the steady-state boundary is determined, the frequency estimates in the stable region are modeled using an autoregressive process. Unlike deterministic polynomial fitting, which assumes a noise-free trend and is prone to edge divergence during backward extrapolation, the AR model jointly captures the smooth frequency variation and the temporally correlated tracking noise inherent in PLL outputs (a quantitative comparison is provided in Section 4.1). Moreover, the AR coefficients are obtained via ordinary least squares without requiring explicit knowledge of the noise statistics, making the approach both computationally efficient and robust under varying INR conditions. A p-th order AR model can be expressed as

$$x(m) = \mu + \sum_{b=1}^{p} \phi_b x(m-b) + e(m) \tag{23}$$

where $x(m)$ $(m > m_0)$ is the estimated frequency value at time m, μ is the intercept term, ϕ_b $(b = 1, \ldots, p)$ are the autoregressive coefficients, and $e(m)$ is a zero-mean noise term. The coefficients are estimated by minimizing the sum of squared residuals:

$$\min_{\mu,\phi} \sum_{m=m_0+p+1}^{N_t} \left(x(m) - \mu - \sum_{b=1}^{p} \phi_b x(m-b) \right)^2 \tag{24}$$

To obtain the AR-based backward-extrapolated frequency estimates during the convergence stage ($m \le m_0$), the AR model in (23) is rearranged to express $x(m-p)$ in terms of subsequent values. Specifically, solving (23) for the earliest term yields a backward recursion from the steady-state region into the convergence region. The backward-extrapolated frequency estimate $\hat{f}_k^{BE}(m)$, $m = 1, 2, \ldots, m_0$, is then given by

$$\hat{f}_k^{BE}(m) = \frac{1}{\phi_p} \left[\hat{f}_k(m+p) - \mu - \sum_{b=1}^{p-1} \phi_b \hat{f}_k(m+p-b) \right] \tag{25}$$

Thus, the compensation function $H_k(n,m)$ is expressed as

$$H_k(n,m) = \begin{cases} \exp\left(j2\pi(\hat{f}_k^{BE}(m) - \hat{f}_k(m))n\right) & m \le m_0 \\ 1 & m > m_0 \end{cases} \tag{26}$$

where n is the sampling point number within a pulse. For $m \le m_0$, the compensation rotates the reconstructed signal phasor from the erroneous frequency $\hat{f}_k(m)$ to the AR-based backward-extrapolated frequency estimate $\hat{f}_k^{BE}(m)$; for $m > m_0$, the tracking loop has converged and no correction is applied. The frequency-compensated interference signal is

$$\hat{y}_{\mathrm{fc},k}(n,m) = \hat{y}_k(n,m) \times H_k(n,m) \tag{27}$$

On the basis of the ARSSC-based reconstructed signal compensation, the frequency error introduced during the iterative convergence process is minimized. To achieve CCI suppression, a subspace projection-based suppression algorithm is developed. A p_l-dimensional interference subspace X is initially constructed

$$\mathsf{X} = \mathsf{B}[\hat{y}_{\mathrm{fc},k}(n)\ \mathsf{P}\hat{y}_{\mathrm{fc},k}(n)\ \cdots \mathsf{P}^{p_l}\hat{y}_{\mathrm{fc},k}(n)] \tag{28}$$

where $\hat{y}_{\mathrm{fc},k}$ is a vector representing the frequency-compensated interference signal, which also constitutes the basis of the subspace. Here p_l denotes the dimension of the projection subspace, which is distinct from the AR model order p introduced in (23). The permutation matrix P is defined as

$$\mathsf{P} = \{p_{ij}\}_{i,j=1\ldots N+p_l-1}, \quad p_{ij} = \begin{cases} 1 & i = j+1 \\ 0 & \text{otherwise} \end{cases} \tag{29}$$

which shifts the signal $\hat{y}_{\mathrm{fc},k}$ by single sampling point, and B chooses the last N rows of the time-delayed interference matrix.

$$\mathsf{B} = \{b_{ij}\}_{i=1\ldots N,j=1\ldots N+p_l-1}, \quad b_{ij} = \begin{cases} 1 & i = j-p_l+1 \\ 0 & \text{otherwise} \end{cases} \tag{30}$$

Based on the interference subspace, a CCI suppression model is established as

$$\min_{\mathbf{w}}\{\|r_{surv} - \mathsf{X}\mathbf{w}\|\} \tag{31}$$

where $\mathbf{w}$ is the projection coefficient vector, which can be derived through differentiation of (31)

$$\mathbf{w} = (\mathsf{X}^H\mathsf{X})^{-1}\mathsf{X}^H r_{surv} \tag{32}$$

Therefore, the interference suppression in the surveillance channel can be accomplished by substituting $\mathbf{w}$ back into (31), and the remaining signal is

$$r'_{echo} = [I_N - \mathsf{X}(\mathsf{X}^H\mathsf{X})^{-1}\mathsf{X}^H]r_{surv} \tag{33}$$

3.3. Flow Chart of GPBR Detection

The flowchart of the proposed GPBR CCI suppression approach is depicted in Figure 7, which consists of two main steps: iterative CCI signal reconstruction (Section 3.1) and ARSSC-based compensation with subspace projection suppression (Section 3.2).

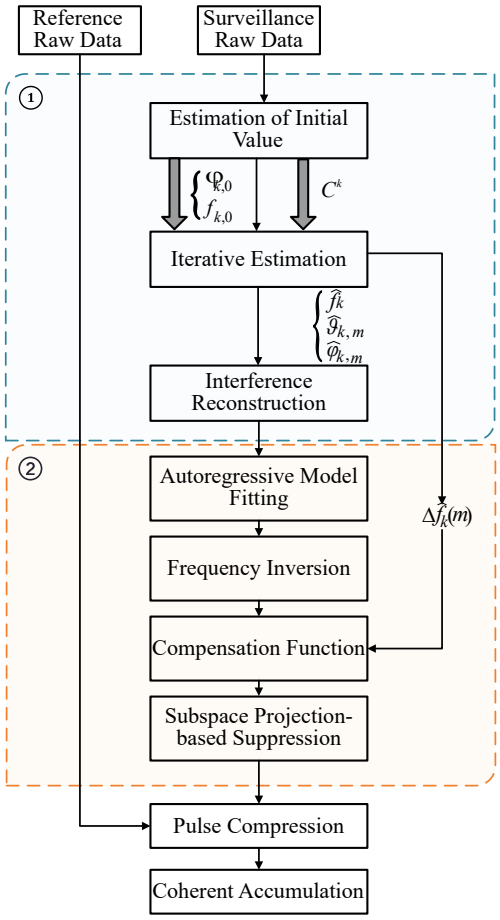


Figure 7. Flowchart of GPBR CCI suppression processing. The numbers **1** and **2** mark the two main steps: (1) iterative CCI signal reconstruction, and (2) ARSSC-based compensation with subspace projection suppression.

3.4. Computational Complexity Analysis

To evaluate the practical applicability of the proposed method, the computational complexity of each processing stage is analyzed and compared with the traditional SRP-based and EASI-based methods.

The proposed ARSSC method consists of four main stages. In the initial parameter search stage, the surveillance signal is cross-correlated with 32 local ranging codes across N_f frequency bins, yielding a complexity of $\mathcal{O}(32 \times N_f \times N)$, where N is the number of sampling points per pulse. In the iterative reconstruction stage, the carrier and envelope parameters of K interference satellites are estimated over N_t pulses, with a per-iteration complexity of $\mathcal{O}(N_t \times N \times K)$. The AR modeling stage fits a p-th order model using M steady-state samples via least-squares estimation, requiring $\mathcal{O}(p^2 \times M)$ operations. Finally, the subspace projection stage constructs a p_l-dimensional interference subspace and computes the projection matrix, with a complexity of $\mathcal{O}(p_l \times N + N \times p_l^2)$ for the matrix inversion and projection.

Table 1 summarizes the computational complexity comparison among the three methods. The EASI method involves iterative matrix updates with a complexity of $\mathcal{O}(I_{EM} \times K^2 \times N)$, where I_{EM} is the number of expectation–maximization (EM) iterations. The traditional SRP method shares the same initial search and iterative reconstruction stages as the proposed method but omits the AR modeling and compensation steps.

Table 1. Computational complexity comparison.

Method	Main Operations	Complexity
EASI	EM iteration	$\mathcal{O}(I_{EM} \times K^2 \times N)$
Traditional SRP	Search + Reconstruction	$\mathcal{O}(32N_fN + N_tNK)$
Proposed ARSSC	Search + Reconstruction + AR + Compensation	$\mathcal{O}(32N_fN + N_tNK + p^2M)$

Compared with the traditional SRP method, the additional overhead of ARSSC is confined to the AR modeling term $\mathcal{O}(p^2M)$, which is negligible relative to the dominant reconstruction term, so the overall complexity scales linearly with the number of interference satellites K. Figure 8 compares the computational load of the three methods as a function of N_t. The EASI method incurs the highest cost owing to its iterative expectation–maximization procedure, whereas the traditional SRP and proposed ARSSC methods exhibit nearly identical loads, confirming that the AR compensation stage adds less than 1% additional computation at the simulation setting of $N_t = 600$.

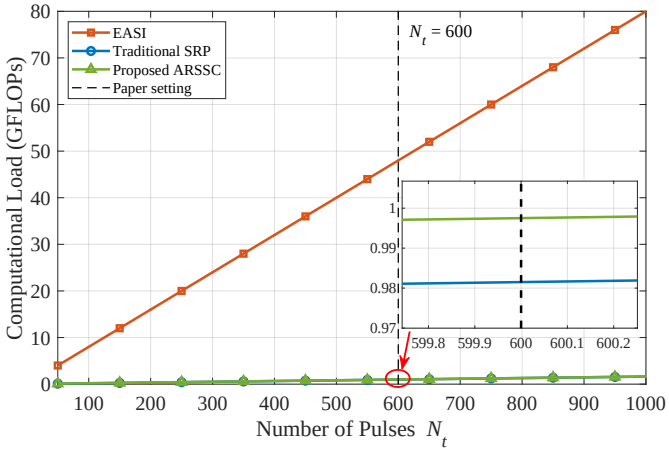


Figure 8. Computational load comparison of EASI, traditional SRP, and proposed ARSSC methods versus the number of pulses N_t.

4. Experiments

To investigate the effect of the proposed method, simulation and measured data-based experiments are conducted in this section.

4.1. Simulation Experiment

The configuration of the computational simulation is set up as closely as possible to real-world conditions. The coordinates and velocities of GPS satellites are determined using actual received ephemeris data. One of the satellites is employed as the radar transmitter for target detection, whereas five other satellites located within the radar mainlobe act as sources of CCI. Further simulation parameters, such as pulse repetition frequency (PRF), are provided in Table 2.

Figure 9 illustrates the trend of the frequency difference $\Delta\hat{f}_k$ in one CCI scenario. It is worth noting that $\Delta\hat{f}_k$ is an estimated value and can only qualitatively represent the magnitude of the error. As shown, the frequency difference exhibits large fluctuations during the initial convergence stage and gradually decreases as the tracking loop stabilizes. After approximately 170 ms, the error value falls entirely below the threshold η_f, indicating that the estimation has entered the steady state. The boundary m_0 identified at this point

partitions the frequency estimates into convergence and steady-state stages, providing the basis for subsequent AR model fitting and backward extrapolation.

Table 2. Simulation parameters.

Parameters		Value	Unit
PBR-transmitter	PRN	24	/
	Coordinate	(−12,164, 16,889, −81,199)	km
	Velocity	(−659, 199, 3056)	m/s
CCI-1	PRN	13	/
	Coordinate	(−12,219, 2763, 17,874)	km
	Velocity	(−389, −2710, 808)	m/s
CCI-2	PRN	5	/
	Coordinate	(−17,751, 2098, 13,586)	km
	Velocity	(−2081, −612, −2056)	m/s
CCI-3	PRN	15	/
	Coordinate	(−4195, 13,435, 14,155)	km
	Velocity	(−1156, −2027, 1784)	m/s
CCI-4	PRN	18	/
	Coordinate	(4760, 10,861, 17,499)	km
	Velocity	(−1959, 1753, −1066)	m/s
CCI-5	PRN	29	/
	Coordinate	(5149, 2081, −4697)	km
	Velocity	(−305, −127, −3189)	m/s
Target	Coordinate	(3, 7, 3)	km
	Velocity	(50, −114, 25)	m/s
PBR-receiver	PRF	1000	Hz
	Bandwidth	1.023	MHz
	Integration time	0.6	s
	Sampling frequency	32	MHz

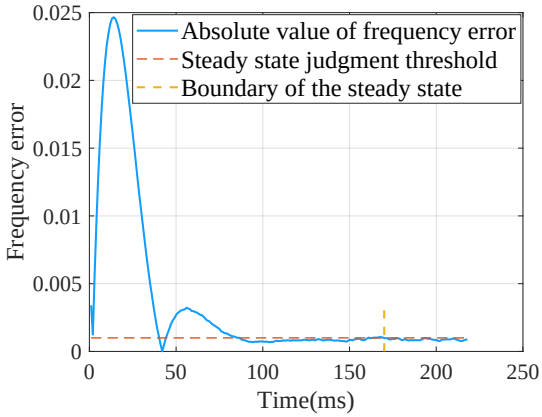


Figure 9. Extraction of the steady-state boundary m_0, using estimated frequency difference and the threshold.

Figure 10 plots the comparison of simulated RD results. The simulation configures a static passive receiver placed on the surface of the earth, and a target is positioned at a bistatic distance of 1.8 km from the receiver, with five CCI satellites positioned along the radar-target line-of-sight extension. Because the CCI signals are coherently accumulated over pulses, they form interference stripes that remain significantly stronger than the target return after coherent integration. Consequently, the interference is focused across all range

units in multiple Doppler cells, as shown in Figure 10a. The SIR after coherent accumulation is calculated by estimating the interference power at the Doppler frequency where the interference is located. The RD results after different processing methods are presented in Figure 10b–d. As observed in Figure 10b, although the EASI method exhibits a certain level of effectiveness, it cannot effectively eliminate the interference in the scenario with five CCIs. The traditional SRP-based algorithm shows better performance compared with the EASI-based blind source separation method, as illustrated in Figure 10c. Utilizing GPS structural information, five CCIs can be effectively identified; however, residual CCIs remain in the RD domain due to frequency errors in the reconstructed CCI signals. Figure 10d shows the RD result with the proposed procedure, where the CCIs are suppressed by over 20 dB, enabling correct target detection.

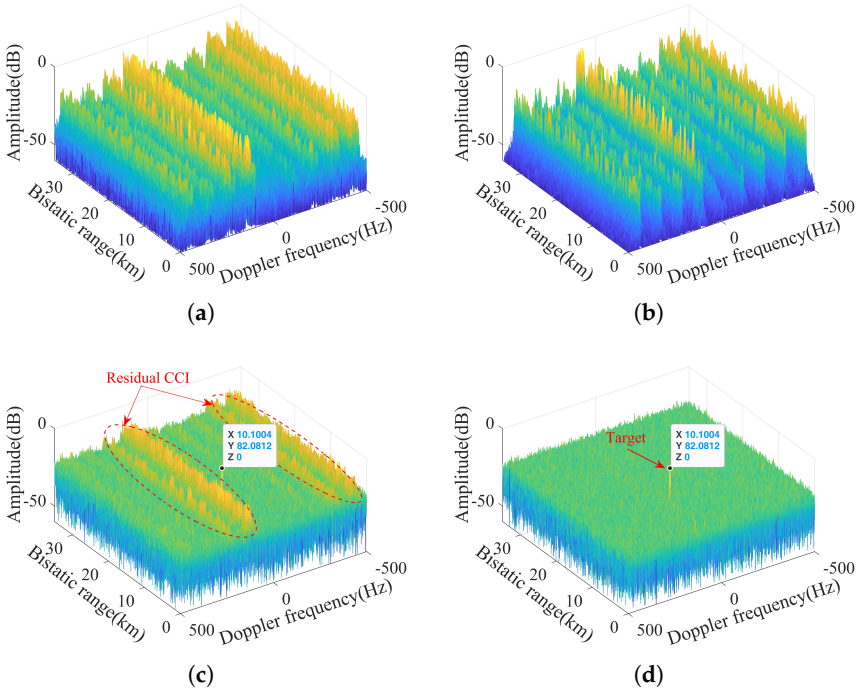


Figure 10. Comparison of the RD results. (**a**) Without interference suppression processing. (**b**) Blind source separation based EASI method. (**c**) Traditional SRP-based method without ARSSC. (**d**) Proposed ARSSC method.

Figure 11 illustrates the interference suppression ratio (ISR) as a function of INR for both the traditional SRP-based method and the proposed ARSSC method, evaluated over 1000 Monte Carlo trials. The ISR is defined as the ratio of the interference power before and after suppression, measured in the range-Doppler domain. As shown, both methods exhibit improved suppression capability with increasing INR, since a stronger interference signal leads to more accurate acquisition and carrier frequency tracking. The traditional method converges rapidly and saturates at approximately 13.2 dB when INR exceeds 3 dB, indicating a fundamental performance ceiling imposed by the residual frequency mismatch between the reconstructed and actual CCI signals. In contrast, the proposed ARSSC method achieves a substantially higher ISR across the entire INR range, reaching a peak of 20.6 dB at INR = 34 dB. At INR = 0 dB, the proposed method attains an ISR of 19.7 dB, yielding an improvement of 6.7 dB over the traditional approach. This advantage increases to 7.4 dB at INR = 40 dB, confirming that the AR-based frequency compensation provides progressively greater benefit as the tracking quality improves. The boxplot distributions further reveal that both methods maintain tight interquartile ranges at moderate-to-high INR levels. At INR = 40 dB, the proposed method exhibits an interquartile range of 0.13 dB, compared

to 0.01 dB for the traditional method. This moderate increase in dispersion is attributable to the sensitivity of AR backward extrapolation to occasional tracking outliers; however, the absolute dispersion remains negligible relative to the 7.4 dB mean improvement.

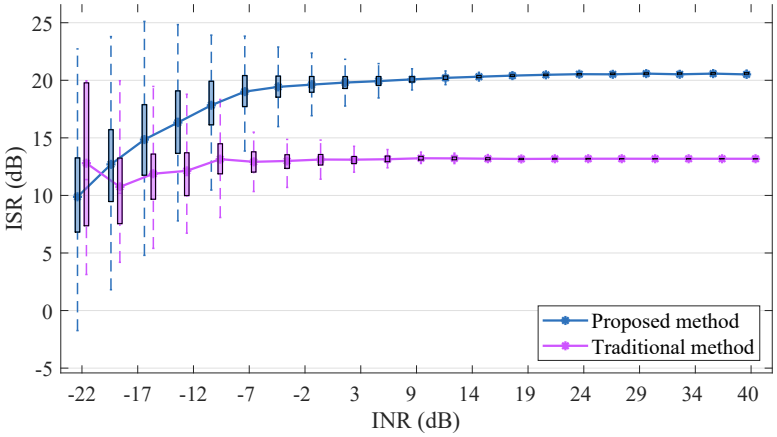


Figure 11. Suppression performance of proposed and traditional methods.

4.2. Steady-State-Based Fitting and Backward-Extrapolation Methods Analysis

To further compare the effectiveness of AR-based frequency backward extrapolation in CCI reconstruction, a module-level experiment is designed using two complementary metrics: frequency root mean square error (RMSE) and divergent-trial rate. The RMSE experiment quantifies the average accuracy of the reconstructed convergence-stage carrier-frequency sequence, whereas the divergent-trial rate is the proportion of Monte Carlo trials whose per-trial RMSE exceeds 10 Hz and is used to characterize extrapolation stability. The comparison includes four frequency-compensation algorithms: ARSSC, Kalman filtering, particle filtering, and polynomial fitting. For each INR value, 1000 Monte Carlo trials are conducted for each method.

All four methods are applied to the same PLL carrier-frequency sequence. The steady-state boundary m_0 is first obtained using the criterion in (22) and is then kept unchanged for all methods, so that the same steady-state segment and the same convergence-stage extrapolation interval are used. The Kalman-filter baseline adopts a second-order frequency state consisting of carrier frequency and frequency rate, with the process and measurement noise settings determined from the steady-state tracking statistics. The particle-filter baseline uses the same state model and noise settings, with 600 particles. The polynomial-fitting baseline uses the same steady-state segment and performs deterministic backward extrapolation over the same convergence-stage interval.

The simulation results are shown in Figure 12. As shown in Figure 12a, ARSSC yields the lowest frequency RMSE throughout the tested INR range, demonstrating that the AR model provides the most accurate convergence-stage frequency reconstruction among the tested algorithms. For example, at INR = 0 dB, its RMSE is 0.70 Hz, compared with 0.75 Hz for the Kalman filter and 0.81 Hz for the particle filter; the polynomial-fitting baseline remains clearly higher because it only captures a deterministic trend and cannot model the temporally correlated tracking-loop errors. Figure 12b further shows that ARSSC has a lower divergent-trial rate under extremely low INR conditions (-20 to -15 dB), indicating better stability when the PLL output is strongly contaminated by tracking noise. As INR increases, the divergent-trial rates of all methods approach zero, and the advantage in this metric becomes less pronounced; thus, the divergent-trial-rate result mainly reveals the robustness margin under the most adverse tracking conditions, while the RMSE result reflects the accuracy advantage across the full INR range.

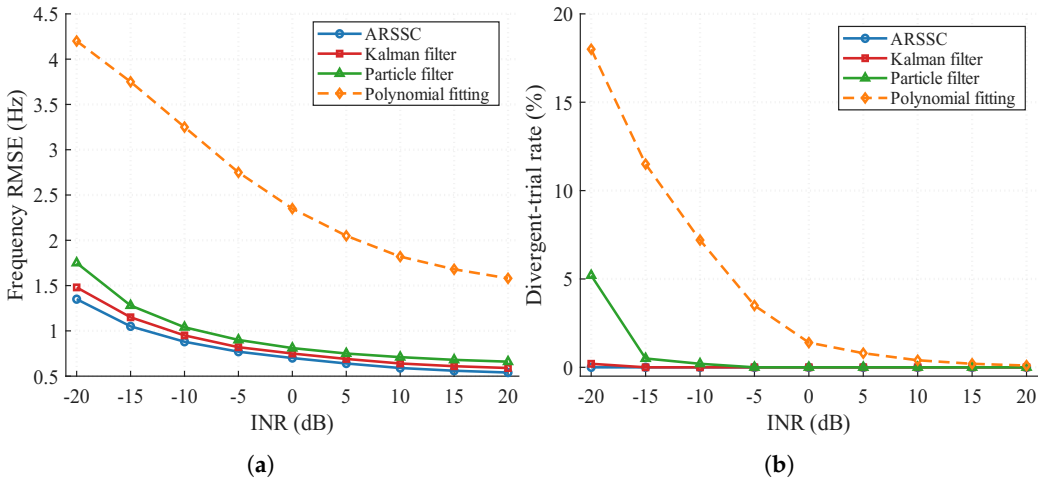


Figure 12. Frequency backward-extrapolation performance comparison of different methods. (**a**) Frequency RMSE versus INR. (**b**) Divergent-trial rate (per-trial RMSE $>$ 10 Hz) versus INR.

Figure 13 further clarifies how different fitting and frequency-backward-extrapolation methods affect the final CCI suppression performance. A unified CCI reconstruction scenario is adopted, in which the receiver geometry, CCI configuration, coherent integration setting, and detection equation are kept unchanged; only the fitting and frequency backward-extrapolation algorithm used for CCI reconstruction is varied. The detection probability is then derived from (10) at $P_{fa} = 10^{-6}$ with 600-pulse coherent integration while sweeping the received SIR. The results show that ARSSC is the most suitable choice for this reconstruction task: at a detection probability of 0.9, it achieves the lowest detectable SIR among the compared methods, whereas Kalman filtering, particle filtering, and especially polynomial fitting require higher received SIR to reach the same detection probability.

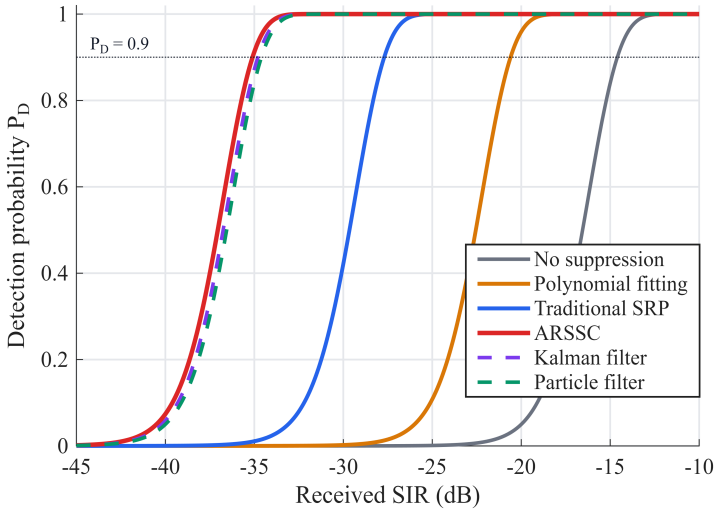


Figure 13. Detection probability versus received SIR for different frequency-fitting and backward-extrapolation methods.

4.3. Parameter Sensitivity Analysis

The performance of the proposed ARSSC method depends on two key parameters: the steady-state boundary threshold η_f and the AR model order p. In this subsection, the sensitivity of the CCI suppression performance to these parameters is analyzed.

4.3.1. Sensitivity to Steady-State Threshold η_f

The threshold η_f in (22) determines the boundary between the convergence and steady-state stages. A smaller η_f yields a more conservative boundary, ensuring that only highly stable frequency estimates are used for AR fitting, but at the cost of reducing the number of available steady-state samples. Conversely, a larger η_f includes more samples but may incorporate residual convergence errors into the AR model, degrading the compensation accuracy.

To evaluate this trade-off, simulations are conducted under the same configuration as Table 2, with five representative values of $\eta_f \in \{0.014, 0.018, 0.022, 0.024, 0.025\}$. The traditional SRP-based method without frequency compensation is included as the baseline. The resulting ISR performance averaged over 1000 Monte Carlo trials is shown in Figure 14.

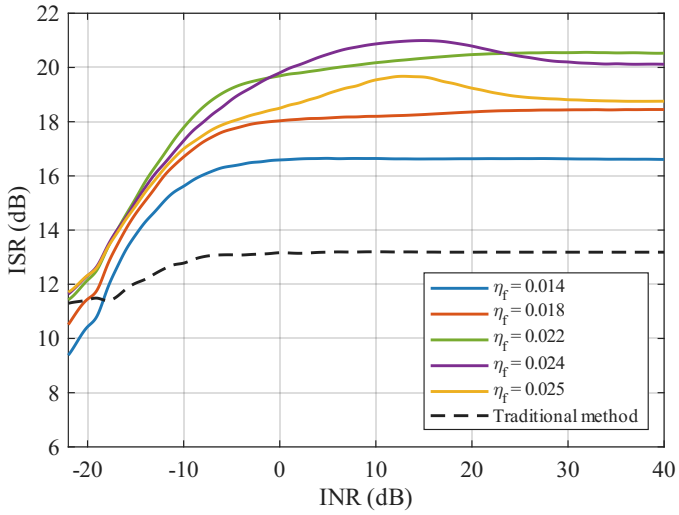


Figure 14. ISR performance versus INR for different steady-state threshold η_f values and the traditional method.

As observed, all five proposed configurations consistently outperform the traditional SRP-based method when INR exceeds -20 dB, and the performance gap widens progressively with increasing INR. The traditional method exhibits early saturation at approximately 13.2 dB, serving as a lower-bound reference. Among the five threshold values, $\eta_f = 0.022$ and $\eta_f = 0.024$ yield the best overall suppression performance, achieving peak ISR values of 20.6 dB and 21.0 dB, respectively. At INR = 0 dB, both configurations attain an ISR of approximately 19.7 dB, corresponding to an improvement of 6.7 dB over the traditional baseline (13.0 dB). A smaller threshold ($\eta_f = 0.014$) leads to an overly conservative steady-state boundary, which excludes a significant portion of usable frequency estimates from the AR fitting process, thereby limiting the ISR to approximately 16.7 dB. Conversely, a larger threshold ($\eta_f = 0.025$) extends the boundary into the convergence region, introducing residual frequency errors into the AR model and degrading the ISR to around 19.9 dB. The results demonstrate that the proposed method is moderately sensitive to the choice of η_f, with a broad effective range of $\eta_f \in [0.018, 0.024]$ yielding consistently high suppression performance. Based on these observations, $\eta_f = 0.022$ is adopted as the default threshold throughout this work, offering a robust balance between model fidelity and sample utilization.

To examine the robustness of the proposed method under dynamic satellite geometry, the following analysis is conducted. In practical deployments, satellite positions vary continuously due to orbital motion, which could in principle challenge the validity of a fixed threshold η_f over successive processing intervals. Within the coherent processing interval employed in this work ($\leq$0.6 s), however, the geometric variation is negligible: the

typical GPS satellite elevation angle changes at a rate below 0.005°/s, corresponding to a Doppler-shift variation far smaller than the robust operating range of $\eta_f \in [0.018, 0.024]$ identified above. The INR sweep in Figure 14 further confirms that $\eta_f = 0.022$ maintains effective suppression across the entire tested INR range of -20 to 40 dB, ensuring robustness against the moderate INR variations induced by elevation-angle changes between successive processing intervals. The 1000-trial Monte Carlo experiment provides an additional, statistically robust confirmation: under the threshold $\eta_f = 0.022$, the divergent-trial rate remains below 1% for INR ≥ -19 dB across all AR orders, indicating that natural variations in interference power are well within the reliability margin. The real-data experiment in Section 4.4, conducted under naturally varying satellite geometry, implicitly validates this conclusion. Nevertheless, scenarios involving sudden interference-power transients—for instance, rapid antenna-pattern changes due to platform rotation—fall outside the scope of the current fixed-threshold design. An online adaptive update of η_f tailored to such time-varying INR conditions is identified as future work.

4.3.2. Sensitivity to AR Model Order p

The AR model order p in (23) controls the complexity of the frequency fitting model. A higher order captures more detailed frequency dynamics but increases computational cost and may lead to overfitting when the number of steady-state samples is limited, while a lower order reduces computational burden but may fail to adequately represent the frequency variation pattern.

To examine AR-based backward extrapolation under different operating conditions, Figure 15 compares the backward-extrapolated estimates against the ground truth for representative p values, under four combinations of INR $\in \{10, -15\}$ dB and $\eta_f \in \{0.022, 0.01\}$. Here, N_{ss} denotes the number of steady-state samples within the valid frequency-tracking segment used for the module-level backward-extrapolation test. As shown in Figure 15a, when an appropriate threshold is chosen ($\eta_f = 0.022$, $m_0 = 72$, $N_{ss} = 65$), all model orders produce backward-extrapolated estimates close to the true frequency throughout the convergence region. In contrast, when the threshold is set conservatively ($\eta_f = 0.01$, $m_0 = 115$, $N_{ss} = 22$, Figure 15b, the reduced sample size degrades the AR fitting, and visible curve dispersion appears at higher orders. The low-INR cases (Figure 15c,d, INR $= -15$ dB) exhibit qualitatively similar patterns but with larger residual errors due to the noisier tracking output.

To rigorously characterize the sensitivity of the frequency backward-extrapolation performance to p and η_f, a Monte Carlo experiment is performed by jointly sweeping $p \in [1, 10]$, $\eta_f \in \{0.022, 0.010\}$, and INR $\in [-22, 40]$ dB. For each parameter combination, 1000 trials are conducted. The same frequency RMSE and divergent-trial-rate metrics are adopted to evaluate extrapolation accuracy and stability, respectively. The corresponding results are presented in Figure 16.

A legitimate concern with AR-based backward extrapolation is whether the model in (23) fits the temporally correlated PLL tracking noise rather than the underlying satellite Doppler dynamics, particularly when the steady-state segment is short. In the proposed framework, this concern is alleviated by design: the length of the AR-fitting segment is governed by the threshold η_f, so that a properly selected η_f retains a sufficient number of steady-state samples N_{ss} for stable AR estimation. Figure 16 provides the empirical validation of this claim.

Figure 16a,b show the frequency RMSE obtained from backward extrapolation. In the low-INR region, lower-order AR models generally produce smaller errors because the fitting data are more strongly contaminated by PLL tracking noise and high-order models are more likely to follow this noise. As INR increases, the steady-state frequency estimates

become cleaner and the benefit of increasing p becomes more visible, especially when the fitting window is shortened by the conservative threshold $\eta_f = 0.010$. The transition between these two regimes occurs around INR = 15 dB. In particular, Figure 16b shows that higher p values can achieve lower RMSE in the high-INR region, indicating that a larger model order is beneficial when the tracking output is sufficiently clean. Under the near-default threshold $\eta_f = 0.022$, however, the available steady-state sample size is sufficient and the RMSE curves for $p \in [1, 4]$ remain close over the entire tested range, indicating that a low-to-moderate AR order is adequate for the proposed compensation task.

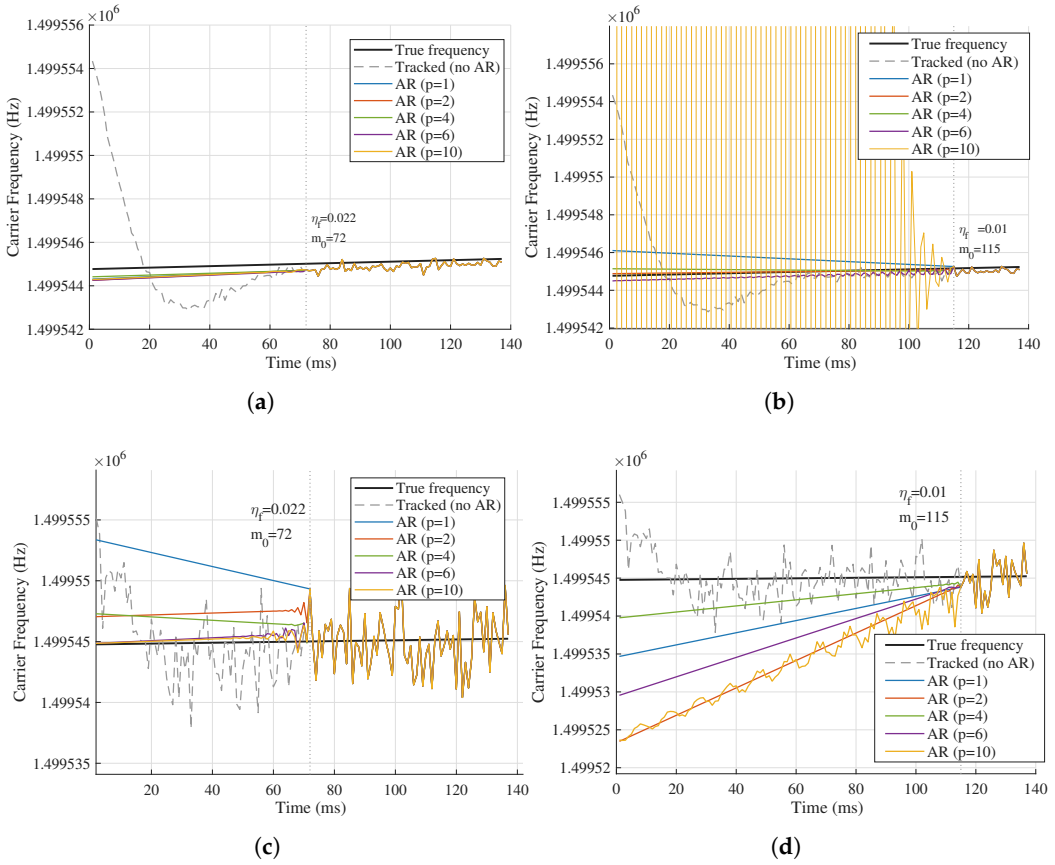


Figure 15. AR-based backward extrapolation under representative operating conditions. (**a**) INR = 10 dB with the threshold $\eta_f = 0.022$. (**b**) INR = 10 dB with the threshold $\eta_f = 0.010$. (**c**) INR = −15 dB with the threshold $\eta_f = 0.022$. (**d**) INR = −15 dB with the threshold $\eta_f = 0.010$.

Figure 16c,d further examine severe error growth caused by unstable extrapolation. For the analysis below, a reliability criterion based on the divergent-trial rate is adopted: the algorithm is considered reliable when the divergent rate remains below 5%, corresponding to the "95% reliability/5% failure tolerance" benchmark widely used in engineering practice. Under the near-default threshold $\eta_f = 0.022$ (Figure 16c), the divergent-trial rate is almost unaffected by p, showing that the AR order does not introduce noticeable overfitting when enough steady-state samples are retained. In contrast, when the threshold tightens to $\eta_f = 0.010$ (N_{ss} reduced from approximately 65 to 22, Figure 16d), a clear rise in divergent-trial rate appears for $p \geq 5$. This confirms that severe degradation occurs mainly under the combined condition of an overly conservative threshold and insufficient fitting samples, rather than being an inherent instability of the ARSSC framework.

Based on these observations, the AR order does not need to be continuously adjusted for each operating condition within the tested range. Instead, Figure 16 shows that $p \in [1, 4]$ provides stable performance under all tested conditions: lower orders are preferable in low-INR or short-window cases, while a moderate order can better capture smooth Doppler

variation when the tracking output is cleaner. Since Figure 16b also indicates that larger p values are advantageous in high-INR conditions, the value $p = 4$ is selected as the default because it is the highest order within the stable range $p \in [1, 4]$, remains below the over-parameterized region observed for $p \geq 5$ under reduced sample size, and still provides sufficient modeling flexibility under high-INR conditions. Combined with the threshold analysis in Figure 14, these results indicate that $\eta_f = 0.022$ and $p = 4$ are suitable recommended values for different operating conditions.

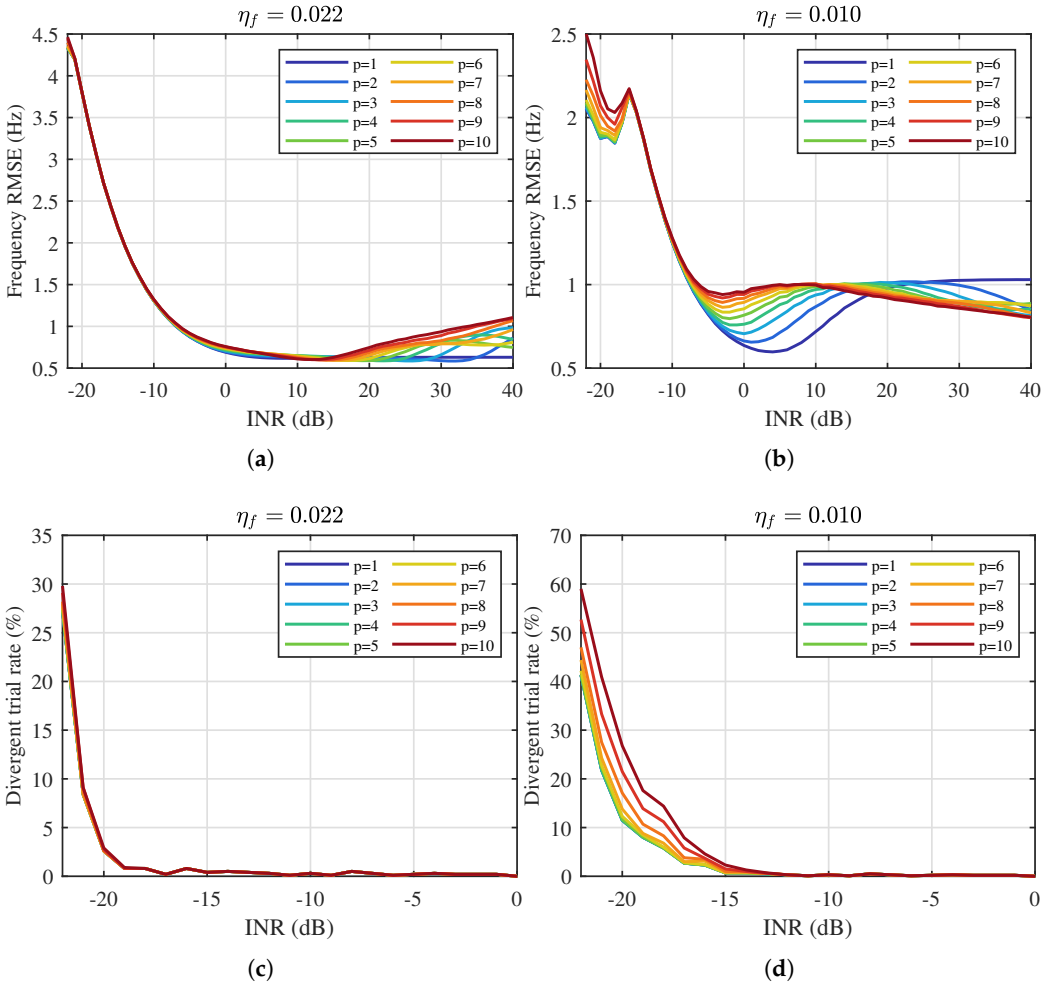


Figure 16. Sensitivity of frequency backward-extrapolation performance to AR model order. (**a**) Frequency RMSE when $\eta_f = 0.022$. (**b**) Frequency RMSE when $\eta_f = 0.010$. (**c**) Divergent-trial rate when $\eta_f = 0.022$. (**d**) Divergent-trial rate when $\eta_f = 0.010$.

Throughout the simulation and real-data experiments in Sections 4.1 and 4.4, the default parameters $\eta_f = 0.022$ and $p = 4$ are adopted.

4.4. Real Data Experiments

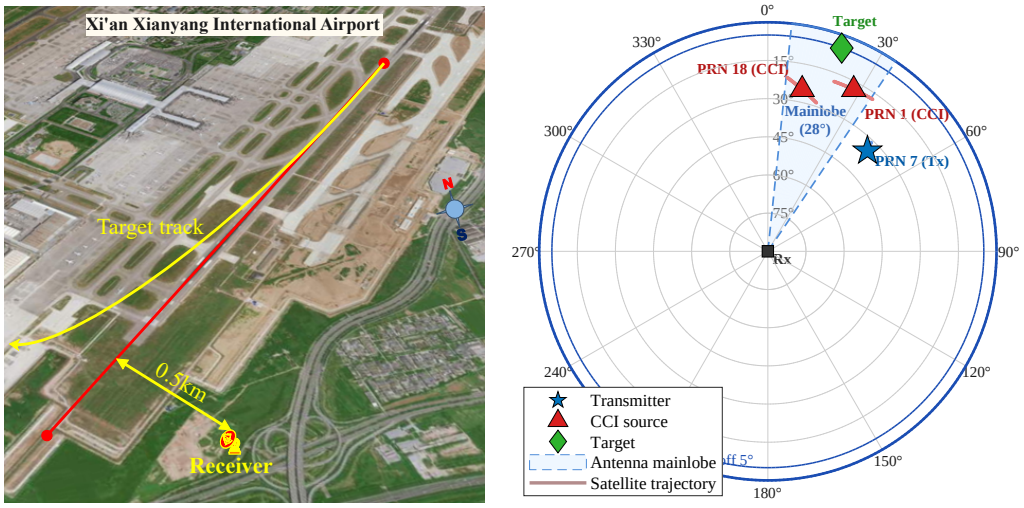
Two field experiments are performed to validate the proposed ARSSC method under different deployment conditions, target types, and interference geometries. The first scenario uses a civil aircraft as the detection target at an airport, with two CCI satellites within the surveillance antenna mainlobe; the second scenario uses a ground vehicle on an open road with four CCI satellites simultaneously present, providing a more challenging multi-source interference environment. Since the interference power cannot be isolated directly in real-data experiments, the ISR is indirectly evaluated via the SIR measured in the RD domain.

4.4.1. First Scenario: Civil Aircraft Detection at Xi'an Xianyang International Airport

A real-data experiment is conducted at Xi'an Xianyang International Airport. As illustrated in Figure 17a, a passive radar receiver is deployed approximately 1 km from the airport runway. The system employs GPS L1 C/A signals as the illumination source, with satellite PRN 7 serving as the radar transmitter. A civil aircraft during takeoff is used as the detection target, located at a range of approximately 1 km from the receiver with a ground speed of roughly 70 m/s. The surveillance antenna is a directional surveillance antenna with a half-power beamwidth of 28°, steered toward the target direction, while a horn antenna serves as the reference antenna for acquiring the direct-path signal from PRN 7.

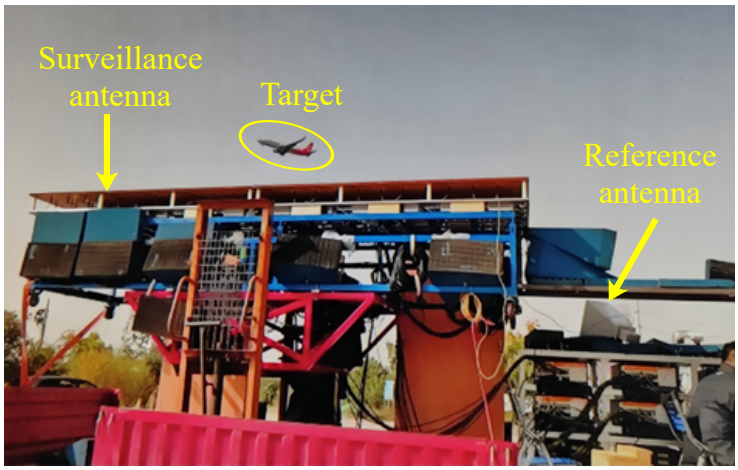
Figure 17b presents a skyplot illustrating the spatial distribution of GPS satellites with respect to the receiver. The surveillance antenna mainlobe, indicated by the shaded sector, covers the angular region around the target. Two interference satellites, PRN 1 and PRN 18, are located within or near the mainlobe, producing significant CCI. The transmitter satellite PRN 7 is positioned at a higher elevation angle in the northeastern sky. The detailed Earth-centered, Earth-fixed (ECEF) coordinates and velocities of all satellites are provided in Table 3.

The received signal is converted to an intermediate frequency and sampled at 32 MHz. Due to the 28° beamwidth, the target echo is only captured intermittently during the aircraft's takeoff trajectory. Within the available data, the segment from 1.95 to 2.2 s is selected for processing, yielding a coherent accumulation time of 0.25 s. The experimental hardware is shown in Figure 18: (a) the antenna configuration at the test site, (b) the radar receiver, and (c) the signal processing board. All the experimental hardware was self-developed by the National Laboratory of Radar Signal Processing, Xidian University, Xi'an, China. Additional system parameters are summarized in Table 3.

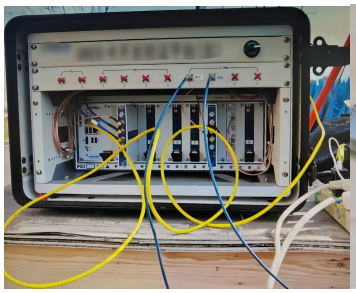


(**a**) (**b**)

Figure 17. Real-data experiment scenario. (**a**) Aerial view of Xi'an Xianyang International Airport showing the receiver location and detection geometry. (**b**) Skyplot of GPS satellite distribution as seen from the receiver; the shaded sector indicates the 28° antenna mainlobe directed toward the target.



(**a**)



(**b**)



(**c**)

Figure 18. Airport experimental setups. (**a**) Experimental scenario and radar antenna. (**b**) Radar receiver. (**c**) Signal processing board.

Table 3. Real data experiment parameters—Airport Scenario.

Parameters		Value	Unit
PBR-transmitter	PRN	7	/
	Coordinate	(−14,843, 3646, 21,373)	km
	Velocity	(1789, −1203, −2051)	m/s
CCI-1	PRN	1	/
	Coordinate	(−4678, 248, 25,981)	km
	Velocity	(−2694, 1198, −497)	m/s
CCI-2	PRN	18	/
	Coordinate	(−9979, −3296, 24,000)	km
	Velocity	(−2724, −326, −1177)	m/s
Target	Coordinate	(1, 5, 3)	km
PBR-receiver	PRF	1000	Hz
	Bandwidth	1.023	MHz
	Integration time	0.25	s
	Sampling frequency	32	MHz

Figure 19 shows the result of the CCI search, which is derived from the normalized amplitude of the cross-correlation between the surveillance channel received signal and the local ranging code. As indicated in the figure, the power levels of the 1st and 18th satellites are significantly higher than those of the others. These satellites are hence identified as sources of CCI in the radar detection.

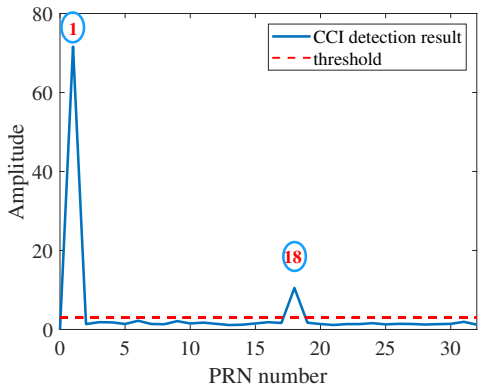


Figure 19. CCI searching result.

Figure 20 presents the RD domain results of the target after range compression and integration, along with other processing steps. In this experiment, the GPS 7th satellite serves as the source illuminator, while signals from the 1st and 18th satellites are received as interference. To enhance visualization, the x-axis of bistatic distance is restricted to a 5-kilometer range due to the proximity of the target, and the y-axis of bistatic velocity is configured to span from -50 m/s to 50 m/s in the RD map to focus on the area near the target. Figure 20a plots the RD result without CCI suppression, where the target is entirely submerged in CCI. This phenomenon occurs because the received CCI signals vary in frequency and contain a large number of multipath components, resulting in correlated interference across different frequency dimensions, which is an important distinction between CCI and traditional interference. Figure 20b,c compare the RD results obtained using the traditional method and the proposed solution. While the traditional reconstruction method significantly reduces the power of CCI, a substantial amount of residual interference remains. In contrast, the proposed ARSSC-based frequency compensation method effectively reduces the residual interference, improving the SIR from -4.76 dB to 13.45 dB, corresponding to a 6.3 dB ISR improvement over the traditional reconstruction method (SIR = 7.11 dB). The EASI method was not applied in the real-data experiment because the number of source signals and their statistical independence—both prerequisites for the algorithm—cannot be reliably determined in a field environment with unknown multipath propagation.

To further assess the practical impact of CCI suppression on target detectability, Table 4 lists the estimated detection probability P_D computed from (10) using the measured SIR values in the RD domain. The SIR prior to suppression is -4.76 dB as observed in Figure 20a. Without any suppression, the detection probability is negligible across all tested false alarm rates, consistent with the severe target masking observed in the RD map. The traditional SRP method raises P_D to 17.6% at $P_{fa} = 10^{-4}$, reflecting the partial interference reduction visible in Figure 20b. In contrast, the proposed ARSSC method achieves $P_D = 99.3\%$ at $P_{fa} = 10^{-4}$ and maintains 93.0% even at the stringent $P_{fa} = 10^{-6}$, confirming that the 6.3 dB ISR gain translates directly into a substantial enhancement in operational target detection performance.

Table 4. Estimated detection probability for the real-data experiment.

P_{fa}	No Suppression	Traditional SRP	Proposed ARSSC
10^{-4}	0.1%	17.6%	99.3%
10^{-5}	<0.1%	7.5%	97.3%
10^{-6}	<0.1%	2.9%	93.0%

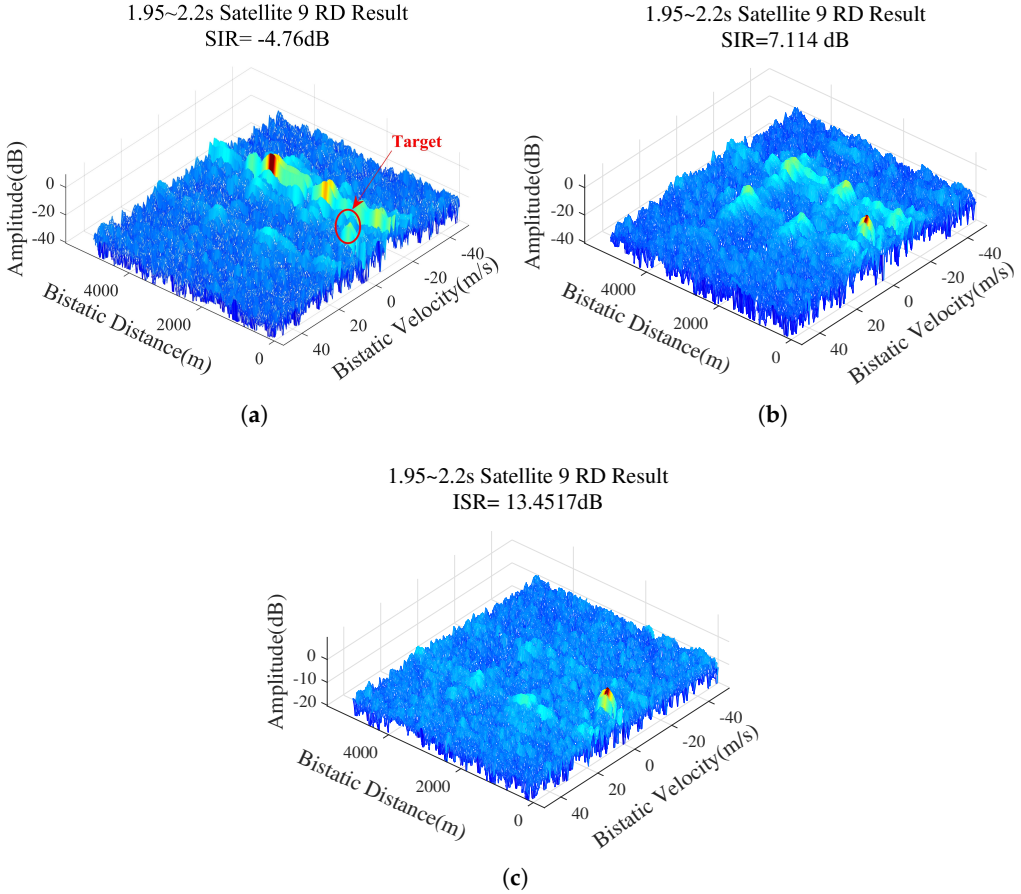


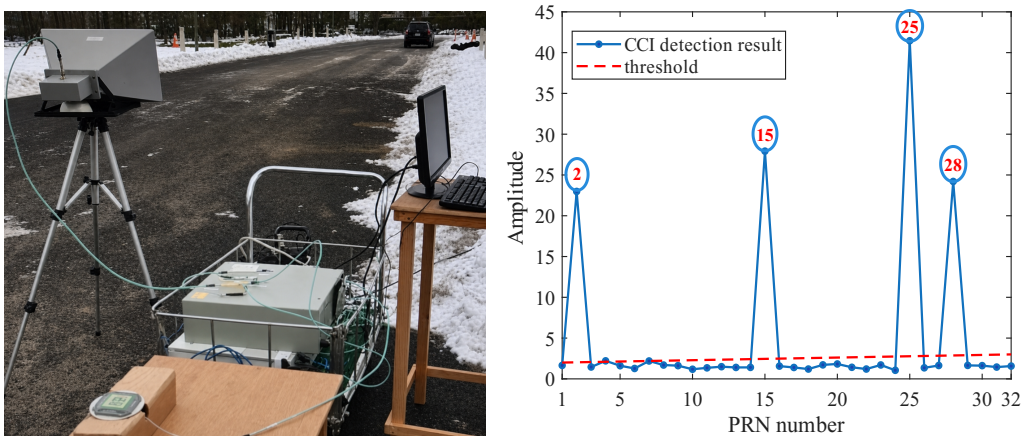
Figure 20. Results of the flight detection trial. (**a**) RD result before CCI suppression. (**b**) Traditional reconstruction method. (**c**) ARSSC-based frequency compensation.

4.4.2. Second Scenario: Ground Vehicle Detection Under Four-Source CCI

To further test the algorithm's adaptability across deployment conditions, target types, and interference configurations, a second real-data experiment is conducted with a ground-vehicle target on a roadway. Four CCI satellites simultaneously fall within the surveillance antenna field of view, yielding a more challenging multi-source interference environment than the two-CCI configuration of the first scenario.

As illustrated in Figure 21a, the passive radar receiver is deployed alongside the roadway, with a directional surveillance antenna mounted on a tripod and steered along the road axis. The surveillance antenna used in this scenario has a half-power beamwidth of 35°, different from the 28° antenna employed in the first scenario. A passenger vehicle traveling along the roadway at approximately 6 m/s is used as the detection target. Figure 21b shows the CCI acquisition result in the surveillance channel, where PRNs 2, 15, 25, and 28 exhibit dominant peak-to-sidelobe ratios and are identified as the four CCI sources.

The system employs GPS L1 C/A signals as the illumination source, with satellite PRN 18 serving as the radar transmitter for this acquisition. The received signal is converted to an intermediate frequency and sampled at 32 MHz, identical to the first scenario. Within the available recording, the segment from 10.9 to 11.15 s is selected for processing, yielding a coherent accumulation time of 0.25 s. The PRNs, ECEF positions, and velocities of the illuminator and the four CCI satellites at the start of the processing interval are summarized in Table 5.



(**a**) (**b**)

Figure 21. Real-data experiment setup and CCI acquisition result for the ground vehicle scenario. (**a**) Experimental setup. (**b**) CCI acquisition peak-to-sidelobe ratio.

Table 5. Real data experiment parameters—Ground Vehicle Scenario.

Parameters		Value	Unit
PBR-transmitter	PRN	18	/
	Coordinate	(−5261, 24,466, −8667)	km
	Velocity	(−261, −1097, −2953)	m/s
CCI-1	PRN	15	/
	Coordinate	(−24,977, −1909, 8754)	km
	Velocity	(−995, −700, −2819)	m/s
CCI-2	PRN	25	/
	Coordinate	(−19,199, 17,356, −5607)	km
	Velocity	(−738, 111, 3069)	m/s
CCI-3	PRN	28	/
	Coordinate	(5446, 25,542, −4873)	km
	Velocity	(−222, 635, 3096)	m/s
CCI-4	PRN	2	/
	Coordinate	(7493, 25,028, 6247)	km
	Velocity	(−125, 736, −3042)	m/s
Target	Coordinate	(0, −0.087, 0.05)	km
PBR-receiver	PRF	1000	Hz
	Bandwidth	1.023	MHz
	Integration time	0.25	s
	Sampling frequency	32	MHz

Figure 22 presents the RD-domain results obtained from the second scenario. Three representative outcomes are compared: the unmitigated result with the four-source CCI present at full strength, the traditional reconstruction-based suppression, and the proposed ARSSC suppression. Figure 22a shows that, without any suppression, the target is completely submerged in the broadband CCI floor, with the SIR collapsing to −24.4 dB. Figure 22b demonstrates the traditional reconstruction-based suppression, which restores the SIR to +3.0 dB—a 27.4 dB ISR improvement over the unmitigated case—but still leaves residual CCI distributed across the Doppler axis due to the imperfect cancellation of the convergence-stage PLL tracking errors. Figure 22c shows the proposed ARSSC method, which elevates the SIR to +9.3 dB, providing an additional 6.3 dB ISR gain over the traditional method under this multi-source configuration; the target appears as a clean peak

with no observable CCI residue. This second scenario thus corroborates the findings from the first scenario and extends the validation envelope of the proposed method to four simultaneous CCI sources.

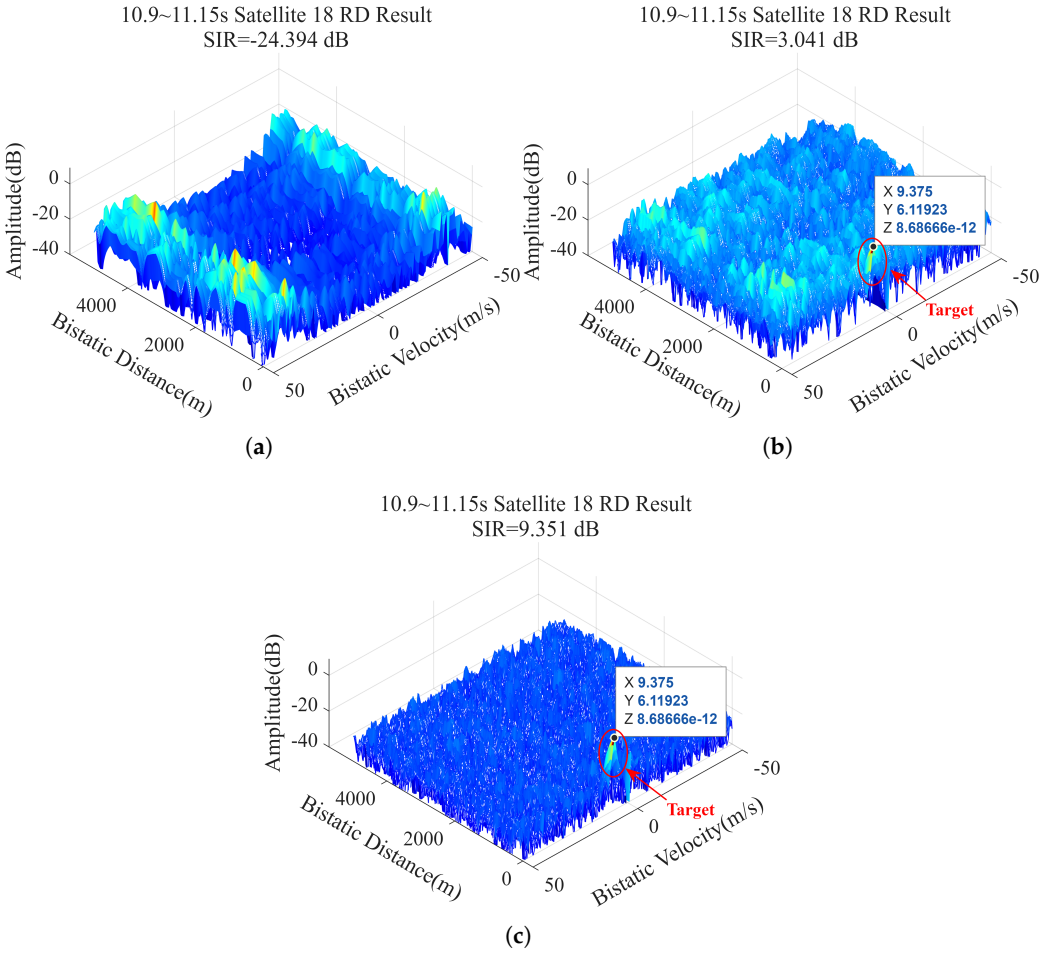


Figure 22. RD-domain results of the ground-vehicle detection trial under four-source CCI. (**a**) Without suppression. (**b**) Traditional reconstruction. (**c**) Proposed ARSSC.

To quantify how the SIR gain translates into target detectability under this more challenging four-source configuration, Table 6 reports the estimated detection probability P_D computed from (10) using the measured SIR values in the RD domain. The absolute P_D values in this scenario are inherently constrained by the lower RCS of the ground vehicle and by the limited coherent integration time available during the segment in which the target remains within the surveillance beam. Within these constraints, the proposed ARSSC method delivers consistently substantial improvements in detection probability over the traditional SRP method across all tested P_{fa} values: from 6.9% to 70.1% at $P_{fa} = 10^{-3}$ (+63.2 percentage points), from 2.0% to 48.1% at $P_{fa} = 10^{-4}$ (+46.2 percentage points), and from 0.5% to 29.0% at $P_{fa} = 10^{-5}$ (+28.5 percentage points). These results correspond to an order-of-magnitude enhancement in detection capability and confirm that the 6.3 dB additional ISR gain provided by ARSSC translates directly into a meaningful operational benefit under multi-source CCI.

Table 6. Estimated detection probability for the ground-vehicle scenario.

P_{fa}	No Suppression	Traditional SRP	Proposed ARSSC	Improvement
10^{-3}	0.3%	6.9%	70.1%	+63.2 pp
10^{-4}	<0.1%	2.0%	48.1%	+46.2 pp
10^{-5}	<0.1%	0.5%	29.0%	+28.5 pp

5. Discussion

The proposed ARSSC framework does not require the receiver platform to be perfectly stationary. It should first be clarified that CCI is the direct satellite-to-receiver signal component received through the surveillance antenna mainlobe; it is not reflected by the target. Therefore, target maneuvering does not change the CCI frequency to be reconstructed by ARSSC. Target acceleration may affect the subsequent target-echo coherent integration, but this is a target-detection issue rather than a CCI-frequency reconstruction issue. For ARSSC, the relevant dynamic factor is receiver platform motion, which introduces both an additional Doppler offset and a small Doppler-rate term through the time variation in the satellite-receiver line-of-sight geometry.

For a moving receiver with velocity $\vec{v}_R(t)$, the CCI Doppler frequency contributed by the k-th satellite can be written as

$$f_{d,k}(t) = \frac{1}{\lambda}\left[\,\vec{v}_{\mathrm{sat},k}(t) - \vec{v}_R(t)\,\right] \cdot \hat{r}_k(t), \tag{34}$$

where $\vec{v}_{\mathrm{sat},k}(t)$ and $\hat{r}_k(t)$ are the satellite velocity and the unit vector from the receiver toward the satellite, respectively. The first term, $\vec{v}_{\mathrm{sat},k} \cdot \hat{r}_k/\lambda$, is the satellite-induced Doppler already handled by the proposed AR-based compensation, while the second term, $\vec{v}_R \cdot \hat{r}_k/\lambda$, is the additional Doppler contribution caused by receiver motion. When $\hat{r}_k(t)$ changes over time, this platform-induced term also contributes a Doppler rate. Using the simulation geometry and a 45° projection angle, the receiver-displacement term alone gives Doppler rates of 0, 4.07×10^{-4}, 1.63×10^{-3}, 3.67×10^{-3}, and 6.52×10^{-3} Hz/s for $|\vec{v}_R| = \{0, 50, 100, 150, 200\}$ m/s, respectively. To avoid underestimating the effect, the Monte Carlo stress test below uses a conservative upper bound that also includes the satellite-motion contribution to the line-of-sight variation.

To quantify this effect, a Monte Carlo experiment is conducted by superposing platform velocities of $|\vec{v}_R| \in \{0, 50, 100, 150, 200\}$ m/s onto the baseline CCI signal at a 45° projection angle. In each case, both the platform-induced Doppler offset and the conservative Doppler-rate bound are injected into the CCI signal. The experiment is performed at INR = 0 dB with 1000 trials per velocity, using $\eta_f = 0.022$ and $p = 4$. As summarized in Table 7, receiver motion changes the absolute CCI Doppler offset by up to 743.2 Hz, while the conservative Doppler rate remains below 0.0310 Hz/s, corresponding to less than 0.0078 Hz of additional Doppler variation within the 0.25 s coherent processing interval. The divergent-trial rate remains at or below 0.1%, and the mean frequency RMSE remains within a few hertz without monotonic deterioration with increasing platform velocity. These results indicate that the additional Doppler offset and geometry-induced Doppler rate introduced by receiver motion have limited impact on the stability of ARSSC frequency extrapolation.

It should also be noted that, although ARSSC cleanly removes the multi-source CCI, the absolute detection probability for small ground targets such as the vehicle considered here remains constrained by the low GNSS power density and the short available integration interval, so reaching operational detection in practice still requires combining ARSSC with long coherent integration [6–11] or multi-source fusion [12] techniques.

Table 7. Frequency backward-extrapolation performance under receiver platform motion, based on 1000 Monte Carlo trials at INR = 0 dB, $\eta_f = 0.022$, and $p = 4$.

$\lvert\vec{v}_R\rvert$ (m/s)	Doppler Offset (Hz)	Doppler Rate (Hz/s)	Mean RMSE (Hz)	Divergent-Trial Rate (%)
0	0.0	0.0000	0.719	0.0
50	185.8	0.0065	0.267	0.1
100	371.6	0.0138	0.471	0.1
150	557.4	0.0220	0.469	0.1
200	743.2	0.0310	0.809	0.1

6. Conclusions

In this paper, we presented the ARSSC method to address the critical yet overlooked challenge of carrier frequency estimation errors in CCI suppression for GPS-based passive bistatic radar. Rather than treating the convergence-stage errors as an inherent limitation of the tracking loop, our approach exploits the smooth, quasi-deterministic nature of satellite Doppler dynamics to extrapolate accurate frequency estimates backward from the steady-state region via a low-order AR model. This purely data-driven compensation strategy requires no prior knowledge of noise statistics or explicit state-space modeling, making it readily applicable across diverse satellite geometries and interference conditions.

Extensive simulations and real-data experiments demonstrate that the proposed method consistently outperforms conventional reconstruction-based approaches. In simulation, the ARSSC method achieves a 7.4 dB ISR improvement over the traditional SRP method, extending the detectable SIR threshold from -27.7 dB to -35.1 dB and substantially expanding the feasible surveillance coverage. An ablation comparison further shows that replacing the AR model with polynomial extrapolation reduces the ISR to only 6.1 dB, confirming the necessity of AR modeling for capturing temporally correlated tracking-loop errors. Real-data experiments under different field scenarios further validate these results, with both the airport aircraft and ground-vehicle scenarios showing a 6.3 dB ISR improvement over traditional reconstruction. In the airport aircraft scenario, this gain elevates the estimated detection probability from 17.6% to over 99% at $P_{fa} = 10^{-4}$. Parameter sensitivity analysis confirms that the default configuration of $\eta_f = 0.022$ and $p = 4$ maintains robust performance across a broad range of operating conditions, with low sensitivity to model order when the threshold is appropriately chosen.

Future work will focus on developing fully online, adaptive parameter selection mechanisms beyond the fixed recommended parameter setting evaluated in this paper, joint multi-CCI frequency modeling that exploits inter-satellite geometric constraints, and extending the framework to multi-constellation Global Navigation Satellite System (GNSS) signals (Galileo, BeiDou, GLONASS)—directions that could further enhance the operational capability of passive radar systems for wide-area aerial surveillance. More broadly, the proposed approach contributes to advancing passive remote sensing based on signals of opportunity, with direct relevance to applications such as air traffic monitoring, border surveillance, and wide-area Earth surface observation, where covert and infrastructure-free sensing is highly desirable.

Author Contributions: Conceptualization, F.X. and S.T.; methodology, F.X. and C.J.; software, F.X. and Z.H.; validation, F.X., C.J. and X.L.; formal analysis, F.X. and F.L.; investigation, F.X. and C.J.; resources, S.T. and L.Z.; data curation, F.X. and Z.H.; writing—original draft preparation, F.X.; writing—review and editing, C.J., S.T. and F.L.; visualization, F.X. and X.L.; supervision, S.T. and L.Z.; project administration, S.T.; funding acquisition, S.T. and L.Z. All authors have read and agreed to the published version of the manuscript.

Funding: This work was supported in part by the National Key Laboratory foundation (2022-JCJQ-LB-006(6142411332207)) of National Key Laboratory of Science and Technology on Space Microwave.

Data Availability Statement: The data are not publicly available due to confidentiality constraints related to the radar system.

Conflicts of Interest: The authors declare no conflicts of interest.

Abbreviations

The following abbreviations are used in this manuscript:

AR	Autoregressive
ARSSC	Autoregressive Steady-State Compensation
BE	Backward Extrapolation
C/A	Coarse/Acquisition
CCI	Cross-Correlation Interference
DPI	Direct-Path Interference
ECEF	Earth-Centered, Earth-Fixed
EASI	Equivariant Adaptive Separation via Independence
EIRP	Effective Isotropic Radiated Power
EM	Expectation-Maximization
GLONASS	Globalnaya Navigatsionnaya Sputnikovaya Sistema
GNSS	Global Navigation Satellite System
GPS	Global Positioning System
GPBR	GPS-based Passive Bistatic Radar
I/Q	In-Phase/Quadrature
ICA	Independent Component Analysis
INR	Interference-to-Noise Ratio
ISR	Interference Suppression Ratio
O-XYZ	Local Cartesian Reference Frame
PBR	Passive Bistatic Radar
PLL	Phase-Locking Loop
PRF	Pulse Repetition Frequency
PRN	Pseudo-Random Noise
RCS	Radar Cross Section
RD	Range-Doppler
RMSE	Root Mean Square Error
SIR	Signal-to-Interference Ratio
SLB	Sidelobe Blanking
SLC	Sidelobe Cancellation
SNR	Signal-to-Noise Ratio
SRP	Software Radio Platform

References

1. Donaldson, J.E.; Parker, J.J.K.; Moreau, M.C.; Highsmith, D.E.; Martzen, P.D. Characterization of on-orbit GPS transmit antenna patterns for space users. *Navigation* **2020**, *67*, 411. [CrossRef]
2. Gronowski, K.; Samczynski, P.; Stasiak, K.; Kulpa, K. First results of air target detection using single channel passive radar utilizing GPS illumination. In Proceedings of the 2019 IEEE Radar Conference (RadarConf), Boston, MA, USA, 22–26 April 2019; pp. 1–6.
3. Van Quan, N.; Markelov, O.A.; Veremyev, V.I. Passive bistatic radar monitoring with GPS satellites as transmitters of opportunity. In Proceedings of the 2021 IEEE Conference of Russian Young Researchers in Electrical and Electronic Engineering (ElConRus), St. Petersburg, Russia, 26–29 January 2021; pp. 1678–1681.
4. Zhang, H.; Liu, W.; Zhang, L.; Meng, Y.; Song, T.; Xu, H.X. Joint resource and trajectory optimization in a UAV-enabled dual-function radar-communication network. *Def. Technol.* **2025**, *in press*. [CrossRef]

5. Zhang, H.; Liu, W.; Zhang, L.; Meng, Y.; Han, W.; Song, T.; Yang, R. An allocation strategy integrated power, bandwidth, and subchannel in a RCC network. *Def. Technol.* **2025**, *in press*. [CrossRef]
6. Pastina, D.; Santi, F.; Pieralice, F.; Bucciarelli, M.; Ma, H.; Tzagkas, D.; Antoniou, M.; Cherniakov, M. Maritime moving target long time integration for GNSS-based passive bistatic radar. *IEEE Trans. Aerosp. Electron. Syst.* **2018**, *54*, 3060–3083. [CrossRef]
7. Pieralice, F.; Santi, F.; Pastina, D.; Bucciarelli, M.; Ma, H.; Antoniou, M.; Cherniakov, M. GNSS-based passive radar for maritime surveillance: Long integration time MTI technique. In Proceedings of the 2017 IEEE Radar Conference (RadarConf), Seattle, WA, USA, 8–12 May 2017; pp. 0508–0513.
8. Santi, F.; Pieralice, F.; Pastina, D. Multistatic GNSS-based passive radar for maritime surveillance with long integration times: Experimental results. In Proceedings of the 2018 IEEE Radar Conference (RadarConf18), Oklahoma City, OK, USA, 23–27 April 2018; pp. 1260–1265.
9. Ma, H.; Antoniou, M.; Pastina, D.; Santi, F.; Pieralice, F.; Bucciarelli, M.; Cherniakov, M. Maritime moving target indication using passive GNSS-based bistatic radar. *IEEE Trans. Aerosp. Electron. Syst.* **2018**, *54*, 115–130. [CrossRef]
10. Zhang, J.; Ding, T.; Zhang, L. Longtime coherent integration algorithm for high-speed maneuvering target detection using space-based bistatic radar. *IEEE Trans. Geosci. Remote Sens.* **2022**, *60*, 5100216. [CrossRef]
11. Ding, T.; Zhang, J.; Tang, S.; Zhang, L.; Li, Y. A novel iterative inner-pulse integration target detection method for bistatic radar. *IEEE Trans. Geosci. Remote Sens.* **2022**, *60*, 5114915. [CrossRef]
12. Pieralice, F.; Pastina, D.; Santi, F.; Bucciarelli, M. Multi-transmitter ship target detection technique with GNSS-based passive radar. In Proceedings of the International Conference on Radar Systems (Radar 2017), Belfast, UK, 23–26 October 2017.
13. Qu, D.; Wang, Z.; Jiang, T. Extended active interference cancellation for sidelobe suppression in cognitive radio OFDM systems with cyclic prefix. *IEEE Trans. Veh. Technol.* **2010**, *59*, 1689–1695. [CrossRef]
14. Richmond, C.D. Performance of the adaptive sidelobe blanker detection algorithm in homogeneous environments. *IEEE Trans. Signal Process.* **2000**, *48*, 1235–1247. [CrossRef] [PubMed]
15. Bandiera, F.; Orlando, D.; Ricci, G. A subspace-based adaptive sidelobe blanker. *IEEE Trans. Signal Process.* **2008**, *56*, 4141–4151. [CrossRef]
16. Guo, S.; Wang, J.; Chen, G.; Wang, J. Mainlobe interference suppression based on independent component analysis in passive bistatic radar. *IET Signal Process.* **2018**, *12*, 1193–1201. [CrossRef]
17. Wang, F.; Wei, S.; Jiang, D. Co-frequency interference suppression for aerostat passive bistatic radar. *Chin. J. Electron.* **2018**, *27*, 658–666. [CrossRef]
18. Gualandi, A.; Serpelloni, E.; Belardinelli, M.E. Blind source separation problem in GPS time series. *J. Geod.* **2016**, *90*, 323–341. [CrossRef]
19. Ge, M.; Cui, G.; Shi, Q.; Kong, L.; Li, N. Mainlobe jamming suppression based on joint blind source separation for distributed radar. In Proceedings of the 2019 IEEE Radar Conference (RadarConf), Boston, MA, USA, 22–26 April 2019; pp. 1–5.
20. Xiang, Y. Blind source separation based on constant modulus criterion and signal mutual information. *Comput. Electr. Eng.* **2008**, *34*, 416–422. [CrossRef]
21. Lei, Z.; Qu, Q.; Chen, H.; Zhang, Z.; Dou, G.; Wang, Y. Mainlobe jamming suppression with space-time multichannel via blind source separation. *IEEE Sens. J.* **2023**, *23*, 17042–17053. [CrossRef]
22. Jutten, C.; Herault, J. Blind separation of sources, part I: An adaptive algorithm based on neuromimetic architecture. *Signal Process.* **1991**, *24*, 1–10. [CrossRef]
23. Novey, M.; Adali, T. On extending the complex FastICA algorithm to noncircular sources. *IEEE Trans. Signal Process.* **2008**, *56*, 2148–2154. [CrossRef]
24. Cardoso, J.F.; Laheld, B.H. Equivariant adaptive source separation. *IEEE Trans. Signal Process.* **1996**, *44*, 3017–3030. [CrossRef]
25. Li, Z.; An, J.; Sun, L.; Yang, M. A blind source separation algorithm based on whitening and non-linear decorrelation. In Proceedings of the 2010 Second International Conference on Computer Modeling and Simulation, Sanya, China, 22–24 January 2010; pp. 443–447.
26. Zhang, J.Y.; Huang, X.X.; Tse, P.W. A comparison of several blind-source-separation algorithms for mechanical signal processing. *Smart Mater. Struct.* **2008**, *21*, 409–416.
27. Schmidt, E.; Ruble, Z.A.; Akopian, D.; Pack, D.J. A reduced complexity cross-correlation interference mitigation technique on a real-time software-defined radio GPS L1 receiver. In Proceedings of the 2018 IEEE/ION Position, Location and Navigation Symposium (PLANS), Monterey, CA, USA, 23–26 April 2018; pp. 931–939.
28. Zheng, H.; Cheng, S.; Zhang, M. Reference signal reconstruction for GPS-based passive radar based on software radio platform. In Proceedings of the 2023 IEEE 6th Information Technology, Networking, Electronic and Automation Control Conference (ITNEC), Chongqing, China, 24–26 February 2023; pp. 732–736.
29. Colone, F.; O'Hagan, D.W.; Lombardo, P.; Baker, C.J. A multistage processing algorithm for disturbance removal and target detection in passive bistatic radar. *IEEE Trans. Aerosp. Electron. Syst.* **2009**, *45*, 698–722. [CrossRef]

30. Zhang, L.; Luo, Y.; Wang, H.; Zhang, Q. Suppression of mainlobe interference in radar network via joint low-rank and sparse recovery. *Trans. Radar Syst.* **2024**, *2*, 303–317. [CrossRef]
31. Zhou, X.; Wang, P.; Zeng, H.; Chen, J. Moving target detection using GNSS-based passive bistatic radar. *IEEE Trans. Geosci. Remote Sens.* **2022**, *60*, 5113415. [CrossRef]
32. Nia, N.K.; Mark, B.L. Models for frequency Doppler shift prediction for LEO satellite communication systems. In Proceedings of the IEEE Military Communications Conference (MILCOM), Rockville, MD, USA, 28 November–2 December 2022; pp. 590–595.
33. Rameez, M.; Dahl, M.; Pettersson, M.I. Autoregressive model-based signal reconstruction for automotive radar interference mitigation. *IEEE Sens. J.* **2021**, *21*, 4454–4463. [CrossRef]
34. Kaplan, E.D.; Hegarty, C. *Understanding GPS: Principles and Applications*, 3rd ed.; Artech House: Norwood, MA, USA, 2017.

Disclaimer/Publisher's Note: The statements, opinions and data contained in all publications are solely those of the individual author(s) and contributor(s) and not of MDPI and/or the editor(s). MDPI and/or the editor(s) disclaim responsibility for any injury to people or property resulting from any ideas, methods, instructions or products referred to in the content.